ACS APPLIED MATERIALS & INTERFACES

www.acsami.org

Forum Article

Magnetic Nanofibrous Hydrogels for Dynamic Control of Stem Cell Differentiation

Md Shariful Islam, Thomas G. Molley, Tzong-tyng Hung, C. I. Sathish, Vina D. L. Putra, Gagan K. Jalandhra, Jake Ireland, Yancheng Li, Jiabao Yi, Jamie J. Kruzic, and Kristopher A. Kilian*

Cite This: https://doi.org/10.1021/acsami.3c07021

Read Online

ACCESS | Metrics & More | Article Recommendations | Supporting Information

ABSTRACT: The extracellular matrix in tissue consists of complex heterogeneous soft materials with hierarchical structure and dynamic mechanical properties dictating cell and tissue level function. In many natural matrices, there are nanofibrous structures that serve to guide cell activity and dictate the form and function of tissue. Synthetic hydrogels with integrated nanofibers can mimic the structural properties of native tissue; however, model systems with dynamic mechanical properties remain elusive. Here we demonstrate modular nanofibrous hydrogels that can be reversibly stiffened in response to applied magnetic fields. Iron oxide nanoparticles were incorporated into gelatin nanofibers through electrospinning, followed by chemical stabilization and fragmentation. These magnetoactive nanofibers can be mixed with virtually any hydrogel material and reversibly stiffen the matrix at a low fiber content (≤3%). In contrast to previous work, where a large quantity of magnetic material disallowed cell encapsulation, the low nanofiber content allows matrix stiffening with cells in 3D. Using adipose derived stem cells, we show how nanofibrous matrices are beneficial for both osteogenesis and adipogenesis, where stiffening the hydrogel with applied magnetic fields enhances osteogenesis while discouraging adipogenesis. Skeletal myoblast progenitors were used as a model of tissue morphogenesis with matrix stiffening augmenting myogenesis and multinucleated myotube formation. The ability to reversibly stiffen fibrous hydrogels through magnetic stimulation provides a useful tool for studying nanotopography and dynamic mechanics in cell culture, with a scope for stimuli responsive materials for tissue engineering.

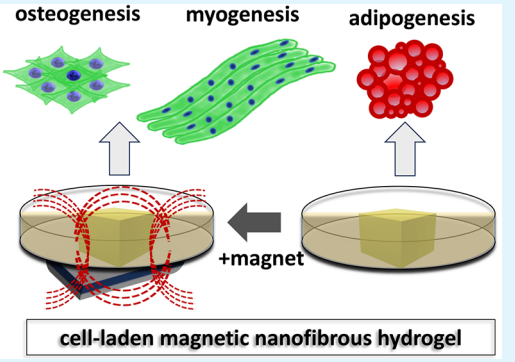

KEYWORDS: *hydrogel, magnetic nanofiber, osteogenesis, adipogenesis, myogenesis*

1. INTRODUCTION

The extracellular matrix presents complex nano- and microtopography to resident cells, with structural and compositional variations across different tissues. The primary aim of tissue engineering is to accelerate the healing process of damaged tissue and to regenerate new tissues, through structural and compositional mimicry.[1,2] Tissue engineering scaffolds must provide initial structural support during the early stage of tissue regeneration including the heterogeneous macro- and nanoscale properties present in the natural tissue, which will assist in generating suitable biochemical and biophysical signals to direct cell growth and differentiation. Tunable scaffold properties are an important characteristic, so that cell behavior can be directed toward preferred differentiation outcomes with spatiotemporal control.[3,4]

Traditionally, the culture of mammalian cells is performed on flat two-dimensional (2D) surfaces, which has provided valuable insight into a broad spectrum of cellular functions like migration, proliferation, and differentiation. However, native tissue is a complex 3D material with heterogeneous intricacy in the presentation of biophysical and biochemical signals. Efforts to understand the multivariate presentation of signals within living tissue has involved control over surface chemistry,[5] substratum mechanics,[6] geometry,[7] and topography.[8] While great strides have been made in developing materials to deconstruct these networks, interrogating multiple complementary and antagonistic pathways remains a principal challenge. Therefore, there is a critical need to create a 3D tissue engineering framework that can mimic the structure and composition of a natural extracellular matrix to direct cell morphology and behavior.

Hydrogels exhibit great potential for 3D tissue engineering scaffolds due to their hydrated network that is similar to natural tissues.[9−11] Even though hydrogels possess properties that are tunable through modifications in the synthesis method,[12] typical hydrogel networks are homogeneous and do not accurately mimic the complex structure found in natural

Special Issue: Materials and Interfaces in Regenerative Medicine

Received: May 16, 2023
Accepted: August 21, 2023

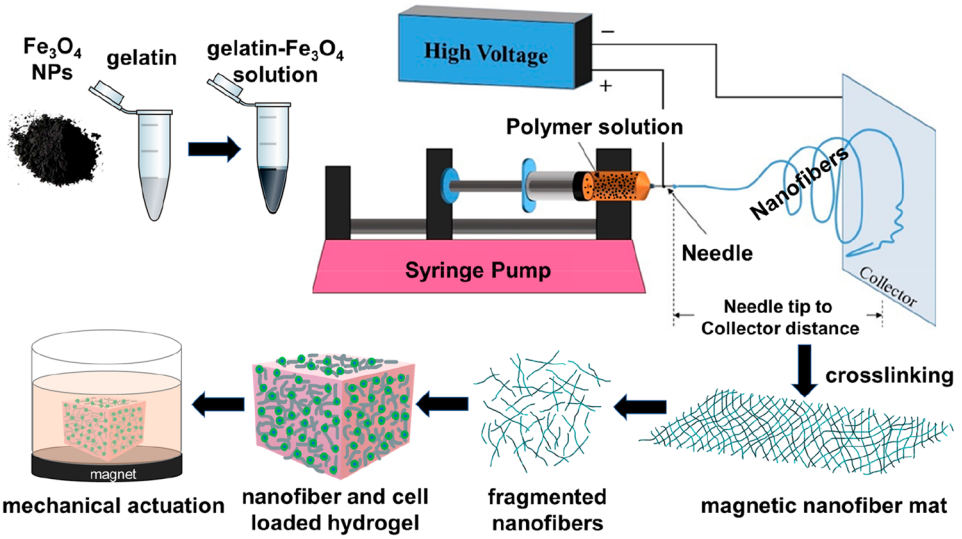

Figure 1. Schematic of the workflow to fabricate magnetoactive hydrogels.

tissues.[7] While some hydrogels are fibrous, fabrication methods rarely accommodate the ordered structure that develops in natural tissue. To address this issue, researchers have explored the integration of nano- and microstructured materials into the 3D network of hydrogels to mimic the heterogeneous structure and physicochemical properties of natural tissues.[13] Adding biomimetic fibers into homogeneous hydrogels has shown great success in mirroring properties of the native matrix.[14−16] Integration of fibers into hydrogels can accommodate various architectures through different assembly means: for instance, layer by layer,[17] rolled,[18] laminated,[19] or blending,[20] with demonstrations of diverse cell outcomes corresponding to the structure. Furthermore, processing conditions can be designed to order the fibers with defined anisotropy that mimics natural structures.[21,22] While these nanofibrous matrices better reflect in vivo tissue structure, they are static systems that do not impart dynamic mechanical stimulation, which is important for many phases of tissue development.

With motivation towards instilling dynamic properties into tissue engineering scaffolds, researchers have developed numerous chemistries where external stimuli can modulate mechanical properties including light,[23−25] pH,[25−27] temperature,[28−30] and magnetic fields.[31−33] Incorporating magnetic nanoparticles into the hydrogel network provides heterogeneity and the remote actuation possibility to mimic dynamic mechanical changes observed *in vivo*.[31,34,35] Furthermore, the magneto-mechanical stimulus provided by an external magnetic field, combined with the anisotropic structure created by a defined distribution of magnetic materials, can be used to regulate the differentiation of cells within the hydrogel network.[36] Although these magnetic hydrogels can be actuated remotely to provide on-demand mechanical signals to cells, these materials fail to mimic the nanofibrous architecture of natural ECMs, e.g., like the fibrous bundles of collagen networks.[37] In recent years, short magnetic nanofibers incorporated into hydrogel systems have shown great potential in tissue engineering,[22,38−40] with resemblance to the native collagen network and on demand remote actuation capabilities.[36]

In this paper, we describe the development of magnetic nanofiber loaded hydrogels for dynamic mechanical stimulation of cells in 3D. Magneto-responsive gelatin nanofibers were synthesized by integrating iron oxide nanoparticles during electrospinning and cross-linked through heat treatment after synthesis. After fragmentation, the fibers were integrated into gelatin methacryloyl hydrogels (GelMa) followed by cross-linking. In contrast to previous magnetoactive materials which require a high content of freely distributed magnetic particles, which could negatively impact 3D cell culture,[41,42] here the particles are sequestered within a small fraction of nanofibers (1−3%) and can reversibly stiffen the material across physiologically relevant ranges allowing mechanical stimulation of cells encapsulated in 3D. We demonstrate the approach by studying differentiation of adipose derived stem cells (ADSCs) and skeletal muscle progenitors when encapsulated within the nanofibrous hydrogels with and without a magnetic field (Figure 1).

2. MATERIALS AND METHODS

2.1. Solution Preparation for the Synthesis of Nanofibers. The synthesis of nanofibers was carried out using a benchtop electrospinning instrument (Bioinicia Ltd., Spain). The electrospinning solution was prepared via the dissolution of gelatin powder with a concentration of 25 wt/v% in a 90% acetic acid (Chem-Supply, AA009) solution. This process was conducted with continuous stirring at 50 °C for 4 h. Subsequently, citric acid (Chem-Supply, CA014) and sodium hypophosphite (Sigma-Aldrich, 10039562) (constituting 15% and 7.5% of gelatin's dry weight, respectively) were added to the mixture by stirring for 2 h. Citric acid served as a cross-linker for the gelatin nanofibers, while sodium hypophosphite acted as a catalyst for the cross-linking reaction.[43,44] To produce the magnetic nanofiber, 5 wt/v% Fe_3O_4 (particle size 50−100 nm, Sigma-Aldrich, 637106) nanoparticles were incorporated into the mixture and were uniformly dispersed using probe sonication (Qsonica Q500, USA) at a 20% amplitude for 1 min. A voltage of 25 kV was consistently applied, along with a needle-to-collector distance of 15 cm and a pump rate of 2 μL/min, to synthesize the nanofibers and collect them on a sheet of aluminum foil. All electrospun solutions were utilized within a seven-day time frame. The process of cross-linking the fibers involved exposing them to a temperature of 150 °C for 4 h using a vacuum oven. The morphology of the nanofibers was assessed using a field emission scanning electron microscopy (FESEM, Hitachi S3400), whereas cross-linking of the nanofibers was confirmed by Fourier transform infrared (FTIR) spectroscopy (PerkinElmer Spectrum Two, USA).

https://doi.org/10.1021/acsami.3c07021
ACS Appl. Mater. Interfaces XXXX, XXX, XXX−XXX

2.2. Short Nanofiber Formation by Sonication. After the fibers were cross-linked in a vacuum oven and manually separated from the collector, they were distributed in 100% ethanol (Chem-Supply, EA043) and broken up with a tip sonicator (Qsonica Q500, USA) at 20 kHz using 50% amplitude. The fragmentation process was carried out for 3 min. Fragmented fibers were then dried in a vacuum oven for 24 h at 50 °C. We used FESEM (Hitachi S3400) to observe the morphology of fragmented fibers. Samples for imaging were prepared by distributing the fragmented fibers over a 12 mm diameter SEM holder and applying a 15 nm platinum coating. ImageJ was used to measure the average length and diameter of the fragmented nanofibers from 100 nanofibers.

2.3. Short Nanofiber Assembled Cell Laden Composite Hydrogel Synthesis. Gelatin methacryloyl (GelMa) powders were synthesized following a method mentioned in the literature.[45] Briefly, type A gelatin sourced from porcine skin (bloom strength 300, Sigma-Aldrich, G2500) was dissolved in phosphate-buffered saline (PBS, pH 7.4, Thermo Fisher Scientific, 10010023) at 10 w/v% under stirring at 50 °C. After that, 5 w/v% methacrylic anhydride (Sigma-Aldrich, 276685) was added, and the mixture was agitated for 90 min. The mixture was diluted twice with 1× PBS and centrifuged at 3000 g for 3 min to remove unreacted methacrylic anhydride. Next, the solution was transferred into 14 kDa cellulose dialysis tubes and dialyzed against deionized water at 40 °C for 5−7 days. Finally, the dialyzed solution was lyophilized for 5−7 days, and the dried powder was stored at −20 °C. Then, 1 and 3 wt/v% short nanofibers were dispersed both in 4 and 8 wt % GelMa solution dissolved in PBS at 37 °C and supplemented with a 0.05 wt % water-soluble photo initiator, Lithium phenyl-2,4,6-trimethylbenzoylphosphinate (LAP, Sigma-Aldrich, 900889). Adipose derived stem cells (ADSCs; 50,000 cells/mL) were dispersed in the fiber-GelMa mixture by pipetting. 100 μL of cell-fiber-GelMa solution mixture was then pipetted within a 6 × 6 × 2.5 mm plastic 3D printed mold placed on a glass slide. Sterilization of the plastic molds was done by first washing the molds with 40% ethanol and then exposing them to UV light for 30 min before adding the gel-fiber-cell mixture. Cross-linking of the composite hydrogel was carried out by a 395 nm UV light torch (100 LED 395 nm UV Ultraviolet Flashlight Blacklight Torch) placed vertically 5 cm apart from the sample and exposed for 1 min. A higher quantity of short nanofibers (≥4 wt/v%) led to unsuccessful cross-linking of the hydrogel samples; therefore, all samples were synthesized using either 1 or 3 wt/v% short nanofibers. Immediately after the cross-linking, cell-laden composite hydrogel samples were placed in a 24 well plate and culturing was continued using 500 μL of cell culture medium. The morphology of the fiber loaded hydrogel composite samples was evaluated by field emission scanning electron microscopy (FESEM, Hitachi S3400) after the samples were dried using a Tousimis Autosamdri-815 critical point dryer. Energy-dispersive X-ray spectroscopy (EDS) mapping was conducted to determine the chemical elements of the samples.

2.4. Evaluating the Mechanical Characteristics and Magnetic Properties of the Hydrogels. Mechanical characteristics of the hydrogel samples were evaluated by an Anton Paar MCR 302 rheometer using a parallel plate geometry with a 25 mm diameter disk, a 1 mm measuring distance, and 600 μL of the gel solution. This study employed oscillatory measurements using a 0.02% strain and a 1 Hz frequency during the gelation process at a temperature of 20 °C. The in situ UV cross-linking method was conducted by introducing a UV light with a wavelength of 395 nm at an intensity of 40 mW/cm^2 for 60 s. The light was positioned underneath the sample to illuminate the sample through the quartz crystal stage.

The investigation of magnetic stiffening of the samples was conducted using a stress-controlled rheometer fitted with a magneto-rheological device capable of administering perpendicular fields up to 1 T in relation to the shear direction. The gel formation process took place within the interstitial region between the rheometer plates, and consequent variations in the storage modulus were registered during the application of a magnetic field ramp ranging from 0 T to 1 T after the hydrogel samples were cross-linked. A magnetic field ramp in the opposite direction (from 1 to 0 T) was employed to assess the degree of reversibility exhibited by the samples.

The magnetic characterization of the magnetic nanoparticle, nanofiber, and hydrogel samples was carried out using VSM (Vibrating sample magnetometer) option in Quantum Design PPMS, USA. Field dependent magnetization curves were measured from −2 to 2 T at 300 K.

2.5. Culturing ADSC and C2C12 Cells in Hydrogel Samples. In all experiments, ADSC (ATCC, PCS-500-011) and C2C12 (ATCC, CRL-1772) cells were encapsulated in the hydrogel samples at a concentration of 50 000 cells/mL. All hydrogel samples were loaded with 500 μL of either proliferation medium or differentiation medium. Medium changes were executed every 48 h. Low-glucose Dulbecco's Modified Eagle's Medium (ThermoFisher Scientific, 11885084) and High-glucose Dulbecco's Modified Eagle's Medium (ThermoFisher Scientific, 11965092) were used as proliferation medium for ADSC and C2C12 cells, respectively. Both mediums were supplemented with 10% (v/v) fetal bovine serum (FBS) (BOVOGEN, Australia, SFBS-AU) and 1% (v/v) penicillin/streptomycin (Sigma-Aldrich, P4333).

For the ADSC differentiation study, the medium was first changed after 48 h and replaced with the differentiation medium. StemPro Osteogenic differentiation media (Thermo Fisher Scientific, A1007201), and StemPro Adipogenic differentiation media (Thermo Fisher Scientific, A1007001) were used for ADSC differentiation as per the manufacturer's instructions.

All cells used in the experiments were between passage 5 and passage 10 and passaged at 70%−80% confluency. To induce a static magnetic field, a neodymium block magnet measuring 25 mm × 12.5 mm × 6 mm and capable of exerting a magnetic flux of 0.36 T was consistently positioned underneath each of the samples for the entire duration of the experiment. A static magnet with a magnetic flux below 0.36 T proved to be insufficient to generate the necessary magnetic force upon our samples.

2.6. Cell Viability Assays. To assess the cell viability, ADSC were encapsulated into the hydrogel samples at a concentration of 50 000 cells/mL. Samples were stained after 12 and 96 h of culture. First the samples were separated from the culture media and washed with PBS. Subsequently a staining solution containing Calcein AM (2 μM, Thermo Fisher Scientific, 65085339) and Ethidium Homodimer-1 (4 μM, Invitrogen, L3224) were added to each sample and incubated in a cell culture incubator for 45 min. Then the samples were washed with PBS and imaged with a confocal microscope.

2.7. Histology Chemical Staining of Composite Hydrogel Samples. All samples were fixed with 4% paraformaldehyde (PFA, Sigma-Aldrich, P6148) at room temperature for 24 h prior to histochemical staining. Alkaline phosphatase and Oil-Red-O staining were performed for classifying osteogenic and adipogenic differentiation, respectively.

Alkaline phosphatase (ALP) staining was carried out by using 5-bromo-4-chloro-3-indolyl phosphate (BCIP) and nitro blue tetrazolium (NBT), a tablet kit (Sigma-Aldrich, B5655). Each tablet was dissolved in 10 mL of deionized water by a tube vortex mixture for 10 min. Fixed gels were then soaked in BCIP/NBT solution for 24 h and washed 3 times with deionized water prior to imaging by a brightfield microscope with a 10× objective.

ALP-stained gels were photographed using a digital camera (Nikon D3400) maintaining uniform lighting conditions and analyzed using Image J.

Oil-Red-O powders (Sigma-Aldrich, 1320065) were first dissolved in 100% isopropyl alcohol (Sigma-Aldrich, 67630) at 3 mg/mL with periodic vortexing for 20 min to make the stock solution. A mixture of stock solution and deionized water (60:40, stock solution: deionized water) filtered by a 0.45 μm filter was prepared for the working solution. Prior to soaking the samples in the Oil-Red-O working solution, gels were soaked for 20 min in 60% isopropyl alcohol in deionized water. After removal of the 60% isopropyl alcohol solution, samples were soaked in working solution overnight at room temperature. Samples were washed three times prior to imaging by a bright-field optical microscope with a 20× objective. To take the

https://doi.org/10.1021/acsami.3c07021
ACS Appl. Mater. Interfaces XXXX, XXX, XXX−XXX

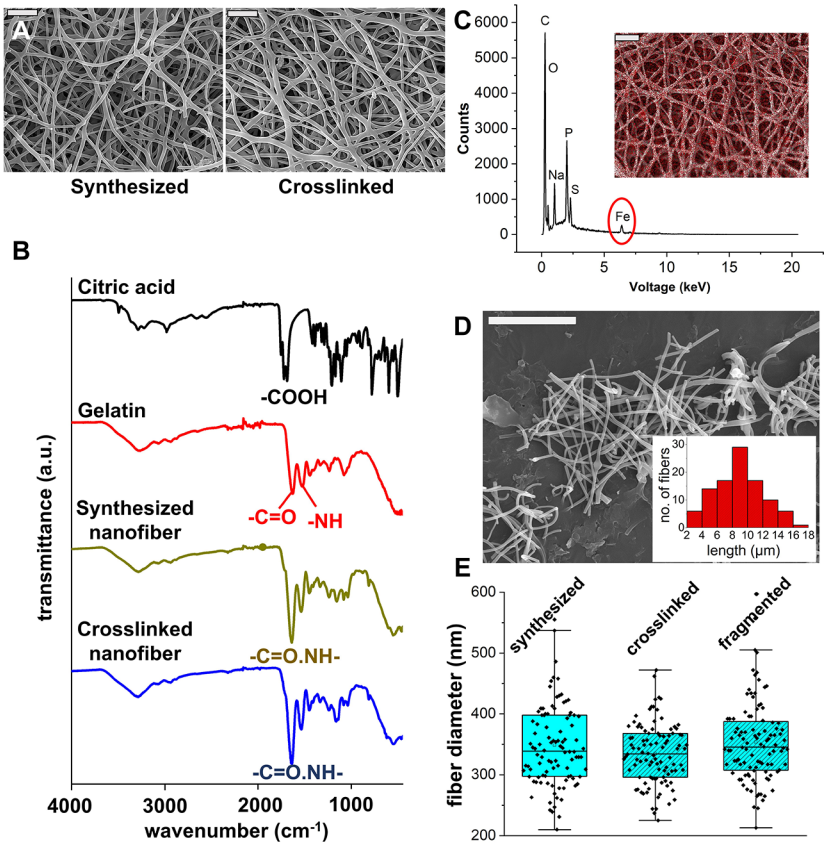

Figure 2. Morphology of magnetic gelatin nanofibers. (A) SEM micrographs of synthesized and cross-linked nanofibers, (B) FTIR spectrum of synthesized and cross-linked nanofibers, (C) EDS mapping of Fe nanofiber distribution across a nanofiber mat, (D) SEM micrographs of fragmented nanofibers and (inset) a histogram of the lengths of the fragmented nanofibers, and (E) fiber diameter distribution of synthesized, cross-linked, and fragmented nanofibers (scale bar = 10 μm and n = 100).

images across the entire length of the samples, each gel was imaged by manually adjusting the focal distances of the different planes. For quantification of the relative amount of lipid droplets in the samples, we counted the total number of lipid droplets present in each sample by manually adjusting the focal distances of the different planes. The area of the samples imaged were 0.25 mm^2. We normalized the total lipid droplets number by comparing it to the total lipid droplets found in control samples.

2.8. Immunostaining of Composite Hydrogel Samples. Samples were fixed with 4% PFA at room temperature for 24 h. After fixing, samples were washed twice with PBS for 1 h. Permeabilization and blocking of the samples were carried out by overnight soaking in 0.5 vol % Triton X-100 (Sigma-Aldrich, 562380) solution and followed by 3 washes with 1 vol % bovine serum albumin (BSA, Sigma-Aldrich, A3858) in PBS for 1 h. Primary and secondary antibody labeling was done in an eppendorf tube by soaking the samples for 24 h at 4 °C. Prior to secondary antibody labeling, samples were washed 3 times with 1 vol % BSA in PBS for 1 h. RUNX-2 (Cell signaling technology, D1L7F), Osteocalcein (Thermo fisher scientific, PA5-96529), FABP4 (abcam, ab92501) and myosin β4 (ThermoFisher Scientific, 14−6503−82) were used as primary antibodies. Composite hydrogels were finally washed 3 times with 1xPBS for 1 h and cleared using cubic-2 clearing solution for 24 h. The cubic-2 solution was prepared by slightly modifying the protocol described in the literature.[46] A mixture of 50 w/v% sucrose (Chem-Supply, 57501) and 25 w/v% urea (Chem-Supply, 57136) was dissolved in deionized (DI) water. When the mixture temperature reached 60 °C, 10% w/v triethanolamine (ThermoFisher Scientific, 121448) was added and stirring was continued for 4 h. Cubic solution was stored at room temperature for up to 4 weeks.

Imaging of the samples was carried out using a Zeiss LSM 800 microscope with either a 10× or 20× objective to see inside the samples. Confocal z-stacks (10× or 20× objective, 25 slices over 100 μm) were recorded for image analysis.

The average cell cytoplasm and nucleus areas, aspect ratios, and roundness of ADSCs were determined by analyzing the actin cytoskeleton with phalloidin staining and the nucleus with 4′,6-diamidino-2-phenylindole (DAPI) staining, respectively, using ImageJ software. At least 100 cells were examined by using ImageJ from three replicate samples. Percentage of RUNX-2 and FABP4 positive cells were calculated by dividing the RUNX-2 and FABP4 positive cells by the total number of cells. To determine the level of osteocalcin expression by the ADSC's after 21 days, the raw intensity of cells that expressed osteocalcin was measured by using ImageJ software after subtracting the background signal.

The average length of the myotubes were measured from three replicates, and all the myotubes present in the samples were counted. To assess the relative expression levels of myosin β4 in the encapsulated cells after 7 days, the myosin β4 image channels were separated, and the intensity was measured using ImageJ software. Furthermore, the fold-increase levels of myosin β4 were determined by normalizing the intensity level of each group with respect to that of the G samples at day 7. Fusion index was calculated by determining the total nuclei incorporated into myotubes in comparison with the total number of nuclei present in the whole image.

2.9. MiroCT Analysis for Evaluating the Mineralization Developed Across the Samples. MicroCT images were taken by a Milabs U-CT scanner (Houten, Netherlands). Prior to placing the samples into the mouse holder of the machine, we sealed fixed gels in parafilm. Images were captured using 50 kV voltage, 0.24 mA current, and 75 ms exposure. Images were analyzed with an Inveon Research

https://doi.org/10.1021/acsami.3c07021
ACS Appl. Mater. Interfaces XXXX, XXX, XXX−XXX

Workplace 4.2 (Siemens, Australia). The extent of mineralization was calculated with a Hounsfield unit (HU) greater than 300 to each gel. The total percentage of the mineralization was calculated by comparing the volume of the particles greater than HU 300 and the total volume of the samples.

2.10. Compression Test of the Unfixed Samples. To evaluate how the compressive stiffness of the samples changed due to the osteogenic differentiation, an Instron ElectroPlus E1000, mechanical test instrument with a calibrated 250 N load cell, was used. The samples were subjected to 25% strain at a test speed of 5 mm/min. Two equations, $\varepsilon_e = \frac{\Delta h}{h_0}$ and $\sigma_e = \frac{F}{A_0}$, were used to calculate engineering strain and stress respectively, where h_o and A_0 are the original height and cross-sectional area of the uncompressed sample, Δh is the change in height, and F is the applied force. The compressive modulus was calculated by finding the average slope of the fitting line for plots of stress versus strain within the 5−10% strain region.

2.11. Isolation of RNAs from Hydrogel Samples for RT-PCR Analysis. Hydrogel samples with ADSC, encapsulated for 21 days in differentiation medium, were first rinsed with PBS and allowed to incubate in a cell culture incubator for 30 min to remove excess media. The samples were then snap-frozen using liquid nitrogen and subsequently turned into a fine powder using mortar and pestle maintaining a cold atmosphere. A RNeasy plant mini kit (Qiagen, 74903) was used to extract RNA from the frozen tissue powder according to the kit's instructions. A High-Capacity cDNA Reverse Transcription Kit (Applied Biosystems, 4368814) was then used to prepare cDNA, which was added to TaqMan Real-Time PCR Master mix (Applied Biosystems, 4304437) with necessary primers and loaded into the wells of a 96 well plate. QuantStudio 7 Flex Real-Time PCR System was used to run the qPCR program, and the software generated automatic cycle threshold (CT) values per replicate, which were converted into ΔΔCT values using GAPDH as an internal control.

2.12. Statistical Analysis. The statistical significance of the results was determined by conducting a one-way ANOVA with Tukey's Post Hoc HSD analysis. Any differences between groups were deemed significant if the P-value was less than 0.05. In the figures, statistical significance was indicated using the following symbols: * for $P < 0.05$, ** for $P < 0.01$, and *** for $P < 0.001$. All whiskers in interval plots and box plots are based on standard deviation (s.d.). To assess the average diameter of the synthesized, cross-linked, and fragmented nanofibers, measurements were obtained from 100 nanofibers from three separate replicate samples. Likewise, the average length of the fragmented nanofibers was determined from 100 fragmented nanofibers derived from three independent replicate samples. The morphometric analysis of the encapsulated ADSC involved the examination of 100 individual cells across three replicates. For the differentiation study, the fraction of positively stained cells was calculated from confocal images by averaging the number of positive cells in z-stacks of 100 μm, with three replicates considered. Additionally, three replicates were employed to measure mineralization contents, conduct compression testing, and assess mRNA expression. Finally, the morphometric analysis of mature myotubes was conducted using three replicate samples as well.

3.3. Results and Discussion. *3.3.1. Characterization of Magnetic Gelatin Nanofibers.* We used electrospinning to synthesize magnetic gelatin nanofibers containing 5 wt/v % iron oxide nanoparticles (Figure 1). This concentration was selected to ensure maintenance of fiber morphology while simultaneously ensuring magnetic response. To stabilize the nanofiber structure, we used a cross-linking method involving citric acid to stabilize the gelatin via amide bonds between strands as previously reported.[43,44] Figure 2 illustrates the morphological characteristics of the synthesized and cross-linked nanofibers. No discernible beads or clusters of polymer spray have been observed in the fibers. The beadless morphology of fibers proves that the integration of magnetic nanoparticles did not impede the process of fiber synthesis. A *Kα* peak at 6.4 eV in the energy-dispersive X-ray spectroscopy (EDS) spectrum proves the presence of Fe in the nanofiber (Figure 2C).[47] Additionally, no localization of the cluster of red dots was detected in EDS mapping (Figure 2C) which provides evidence of particles throughout the fiber mat, with negligible aggregation.

It can be observed from Figure 2A that following the cross-linking process, the fibers retain their fibrous morphology. Before cross-linking, the mean diameter of fibers was observed to be 348 ± 70 nm. Cross-linking using heat treatment did not significantly alter the average fiber diameter (with measurements of 334 ± 49 nm). This observation indicates that the utilized cross-linking method did not diminish the inherent fibrous morphology, which is consistent with previous findings.[44,48,49]

To ascertain the efficacy of the cross-linking process, we have conducted an FTIR analysis of the synthesized and cross-linked nanofibers (Figure 2B). Citric acid exhibits a characteristic band of the carboxylate/carboxylic acid groups (−COOH) in the 1685 cm^{-1} to 1715 cm^{-1} region[49,50] and gelatin exhibits a characteristic band of amide I and amide II at 1628 cm^{-1} and 1525 cm^{-1}, respectively.[51] The synthesized and cross-linked nanofiber samples demonstrate a broad band at 3200 cm^{-1}, which corresponds to the hydroxyl (−OH) and amino groups ($-NH_2$).[52] Furthermore, it is noteworthy that peaks within the spectral range of 1685 cm^{-1} to 1715 cm^{-1} decrase to background in the cross-linked nanofiber samples (Supporting Figure 1A).[53] Theoretically, it is feasible for both amide and imide formations to occur during this reaction.[49] However, the absence of a peak at 1770 cm^{-1} corresponding to imide indicates a successful amide formation in the nanofibers. This is confirmed by the sharp peak observed within the range of 1620 cm^{-1} to 1645 cm^{-1}.[54] A change in the position of amide I (1628 cm^{-1} to 1637 cm^{-1}) and amide II (1525 cm^{-1} to 1534 cm^{-1}) is attributed to formation of amide crosslinks. These peaks exhibited a further shift in the cross-linked nanofiber sample (Supporting Figure 1), thereby signifying that the application of thermal energy expedites the cross-linking process.[50]

The electrospinning method is well-known for creating very compact layers of long nanofiber mats.[55,56] Therefore, it is important to fragment the fibers into the desired size to aid uniform incorporation and dispersion into a hydrogel system. Probe sonication is a technique that utilizes high-frequency sound waves to break down these long fibers into smaller fragments, maintaining the physical morphology and chemical properties, while the fiber length is reduced. The FESEM micrographs indicate that the fragmented short fibers retained their original fiber morphology without noticeable damage to individual fibers (Figure 2D). Additionally, the average fiber diameter remains unchanged even after the fragmentation and drying processes (Figure 2E). Using probe sonication, we were able to achieve an average nanofiber length of 8.9 ± 3.1 μm, with a narrow length distribution (Figure 2E). This finding is consistent with previously published reports, which have also demonstrated the effectiveness of probe sonication in reducing nanofiber length within the range of 8−20 μm.[38,57,58] Further studies have also suggested that fibers with lengths ranging from 8 to 12 μm are suitable for homogeneously distributing inside hydrogels.[57,58] However, tailoring the solution conditions and sonication parameters can help in tuning the size and polydispersity of fragmented nanofibers. In all experiments conducted in this study, fragmented nanofibers were integrated into the hydrogel system at concentrations of 1 and 3 wt/v %. These hydrogels are referred to as G+1F and G+3F, respectively, throughout the manuscript. The notation "G" is used to represent the hydrogel without fibers. Furthermore, to account for the presence of magnetic fields during the experiments, the samples are labeled as G +M, G+1F+M, and G+3F+M, indicating the hydrogel in the presence of a magnetic field "M" without fibers, the hydrogel with 1 wt/v% incorporated fibers, and the hydrogel with 3 wt/v% incorporated fibers, respectively.

3.3.2. Nanofiber Incorporation Influences Overall Storage Modulus of the Bulk Hydrogel. After successfully fragmenting the fibers, we evaluated the morphology and rheological properties of the bulk hydrogel after integrating fibers to understand how the distribution of short nanofibers influences the hydrogel's morpho-

https://doi.org/10.1021/acsami.3c07021
ACS Appl. Mater. Interfaces XXXX, XXX, XXX−XXX

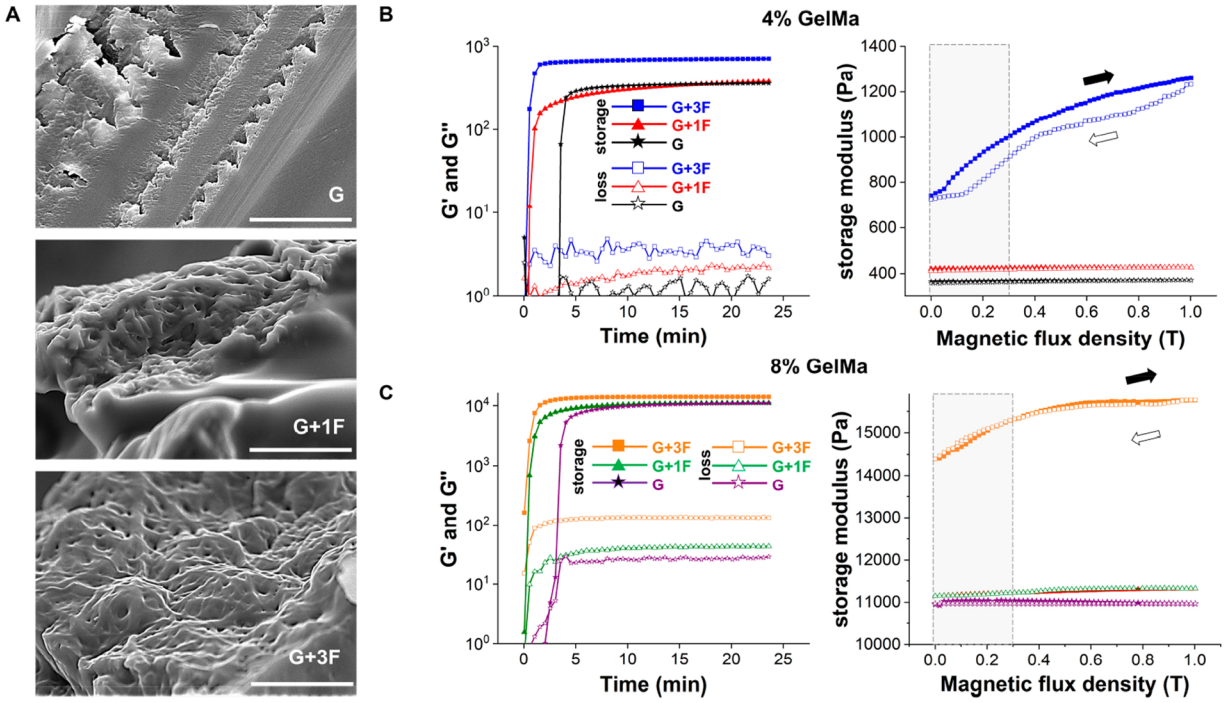

Figure 3. Morphology and mechanical properties of the hydrogel samples. (A) Representative FESEM micrographs of gel samples (G, G+1F, and G+3F) and rheological analysis of gel samples (G, G+1F, and G+3F) synthesized with (B) 4% GelMa and (C) 8% GelMa. In B and C, the left column represents changes in storage (G', solid filled shapes) and loss modulus (G'', hollow shapes) of the gels over time and the right column represents changes in storage modulus when a range (0 to 1 T, solid filled shapes, and 1 to 0 T, hollow shapes) of magnetic field is applied to the cross-linked samples. The boxed region corresponds to the magnetic flux density achieved due to static magnetic field. Square, triangle, and star shapes represent G+3F, G+1F and G, respectively. (scale bar = 20 μm).

logical and mechanical properties. Figure 3A shows the FESEM micrographs of the gel samples. Although the fibrous structures were observable in the G+1F and G+3F samples, distinguishing between the fibers and the bulk gels proved challenging, likely because the fibers and surrounding gel are the same material, thereby not providing sufficient contrast. This difficulty arose from the entanglement of fibers and bulk gels during the drying process, which hindered their differentiation. To evaluate the distribution of magnetic nanofibers within the samples, we performed energy-dispersive X-ray spectroscopy (EDS) mapping (Supporting Figure 2). The EDS mapping confirmed the presence of iron in the G+1F and G +3F samples, providing evidence for the successful integration of the fibers within the gels. Furthermore, the uniform distribution of iron that increased with fiber content demonstrates the uniform distribution within the bulk. Next, we evaluated the rheological properties of the gel samples. Figure 3B, C illustrate the changes in the storage (G': black) and loss (G'': red) modulus over time for GelMa hydrogels with or without fragmented Gelatin nanofibers during UV-cross-linking. In all samples, a steep increase in G' was observed as soon as the UV light was illuminated, indicating the beginning of cross-linking, and it reached a plateau within a few seconds. The storage moduli of G and G+1F samples remain almost the same. However, inclusion of the 3 wt/v% nanofibers (G+3F samples) increased the storage modulus (0.40 to 0.74 kPa in 4% GelMa, 3.55 to 4.53 kPa in 6% GelMa and 10.8 to 14.4 kPa in 8% GelMa). This increase in modulus can be attributed to the stiffness of the nanofibers and the fact that their inclusion did not affect the cross-linking reaction.[59] The viscoelastic response of the polymer network depends upon the polymer chains and the type of applied motion, and the interaction between GelMa and fragmented fibers in the composite hydrogel system may restrict the movement of the polymer chains, leading to yield stress. Similar reports have been found in literature that discuss how fiber contents in hydrogels lead to an increase in the storage modulus.[38,60]

Next, we investigated the effect of a static magnetic field on the mechanical properties of the hydrogels. None of the gel (G) samples exhibited any response to the applied magnetic field. When a ramp of magnetic field (0 T to 1 T) was applied, the samples with a fiber content of 1% (G+1F) display a negligible enhancement in their storage modulus. Conversely, the samples containing 3% fiber content (G+3F) demonstrate a significant enhancement in their storage modulus (69%, 23% and 10% increase in 4%, 6%, and 8% GelMa samples, respectively). The static magnets we used in our experiments were able to exert a 0.3 T magnetic flux density. When 0.3 T magnetic field was applied, 36%, 16%, and 7% increases in storage modulus were observed in 4%, 6%, and 8% GelMa samples, respectively, each containing 3% fiber contents.

All fiber-laden gels (G+1F and G+3F) reverted to their initial storage modulus when subjected to 0 T, indicating that the application of a magnetic field did not elicit any permanent changes to the specimen response. Hysteresis was observed in all samples upon gradual reduction of the applied magnetic field from 1 to 0 T. The forces acting on the magnetic nanofibers within the hydrogels may lead to the reorganization of the fibers within the hydrogel network.[42] However, upon reduction or reversal of the external magnetic field, the realignment process of the magnetic nanofibers is impeded by internal energy barriers, necessitating a sufficient amount of time for them to revert to their original state.[61] During the magneto-rheological testing, no additional time was allocated for the samples to restore their initial arrangement once the external magnetic field was gradually withdrawn. This temporal constraint limits the system's immediate return to its initial state, thereby resulting in the observed hysteresis behavior.[61] To further explore the effect of magnetization, field-dependent magnetic measurements were performed on magnetite nanoparticles, synthesized magnetic nanofibers, and dried hydrogel (G+1F and G+3F) samples made with 8% GelMa (Supporting Figure 3). All the samples show small coercivity (Supporting Figure 3B), confirming their weak ferrimagnetic

https://doi.org/10.1021/acsami.3c07021
ACS Appl. Mater. Interfaces XXXX, XXX, XXX−XXX

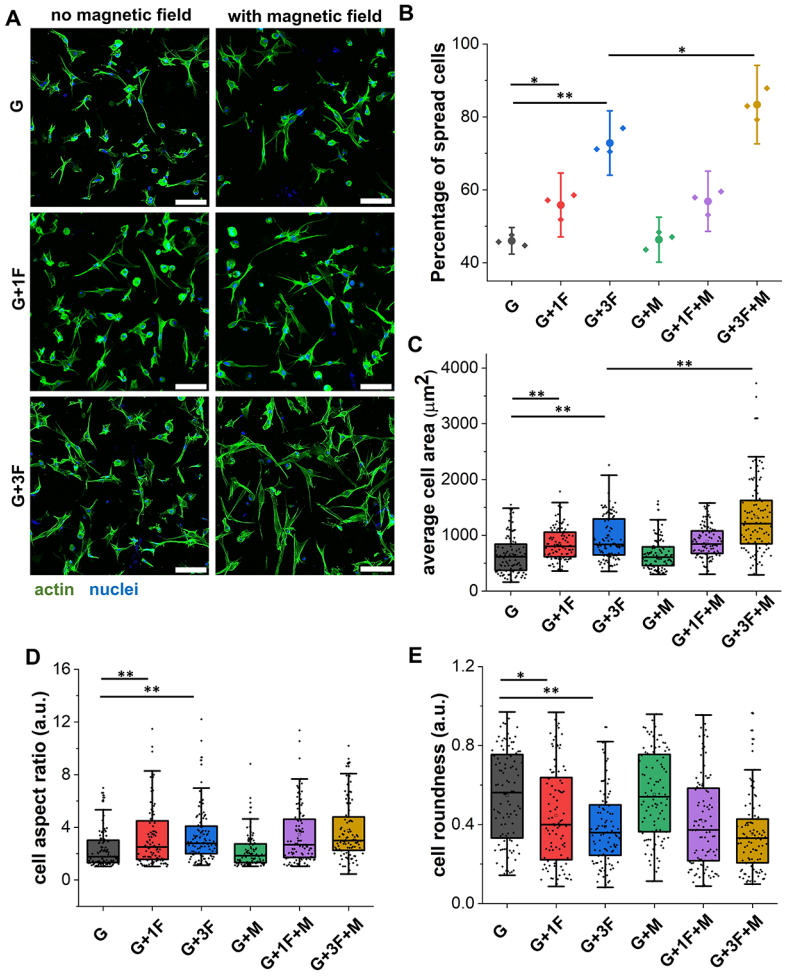

Figure 4. Morphology of ADSCs encapsulated in different hydrogel (8% GelMa) samples for 48 h. (A) Representative confocal z-stack projection images (25 slices over 100 μm) of actin and nuclei represent incorporation of fibers into hydrogel network that led to elongated cellular morphology; (B) percentage of spread cells across different samples; plots for cellular morphology: (C) average cell cytoplasm area, (D) cell aspect ratio, and (E) cell roundness (scale bar = 100 μm, n = 100).

behavior.[62,63] Typically, ferrimagnetic Fe_3O_4 nanoparticles with a particle size ranging from 50 to 100 nm exhibit small coercivity at 300 K.[62,63] Given that the G+1F and G+3F samples were fabricated by incorporating magnetic nanofibers composed of ferrimagnetic Fe_3O_4 nanoparticles, this integration could account for the observed hysteresis in the magneto-rheological measurements of the G+3F samples (Figure 3B, C). The saturation magnetization was found to be 74.3, 8.5, 0.022, and 0.88 emu/g for magnetite nanoparticle, synthesized magnetic nanofiber, dried G+1F and dried G+3F samples, respectively. Higher saturation magnetization of the G+3F samples compared to G+1F samples is reflective of the presence of a higher concentration of magnetic nanofibers. Magneto-rheological measurement also supports this result, as G+3F samples exhibited higher change in storage modulus upon applied magnetic field (Figure 3B, C). We note that the saturation magnetization and the rheological properties after attenuating a field are lower than expected for the G +1F compared to the G+3F. We believe this discrepancy is attributed to heterogeneity in nanofiber distribution and the potential for agglomeration, which could lessen the magnetization and corresponding change in modulus for the condition with a lower quantity of nanomaterials.

3.3.3. Influence of Fiber Content and Substrate Stiffening in ADSC Morphology and Differentiation. Adipose derived stem cell (ADSC), the largest source of easily isolatable adult stem cells,[64] are widely used for regenerative medicine and tissue engineering as they can self-renew and differentiate into various cell types, such as osteoblasts,[65,66] adipocytes,[67,68] chondrocytes,[69,70] and smooth muscle cells.[71,72] A major challenge in this field is guiding their differentiation into specific cell types and maintaining their specialized characteristics in synthetic 3D environments, such as model tissue scaffolds. To address this issue, we have used fiber loaded gels to evaluate the differentiation potential of ADSC into osteogenic and adipogenic linage. In this study, we investigated the impact of adding fiber fragments and stiffening using static magnets on the ADSC morphology and differentiation. Previous studies have shown that hydrogels with a modulus greater than 4 kPa are suitable for osteogenic differentiation, while those with a modulus smaller than 4 kPa are more conducive to adipogenic differentiation.[73,74] In this study, we have used 8% GelMa hydrogels with a modulus of approximately 11 kPa as a control group for differentiating ADSC into osteogenic linage and 4% GelMa hydrogels with a modulus of approximately 0.4 kPa as a control group for adipogenic linage.

3.3.3.1. Changes in Fragmented Fiber Contents and Substrate Stiffening Influence ADSC's Morphological Properties. We encapsulated ADSCs at a concentration of 50000 cells/mL within the following samples: G, G+1F, G+3F, G+1F+M and G+3F+M samples, made with 8% GelMa solution. To modulate the mechanical properties of the hydrogels, we placed a single magnet at the underside of each sample for the duration of the experiment. After cell encapsulation, live dead assays were conducted at two time points: 12 and 96 h, to test the cytocompatibility of the composite materials. We found the cell viability was ≥92% at 12 h and ≥90% at 96 h (Supporting Figure 4) across all tested samples. These results indicate

https://doi.org/10.1021/acsami.3c07021
ACS Appl. Mater. Interfaces XXXX, XXX, XXX−XXX

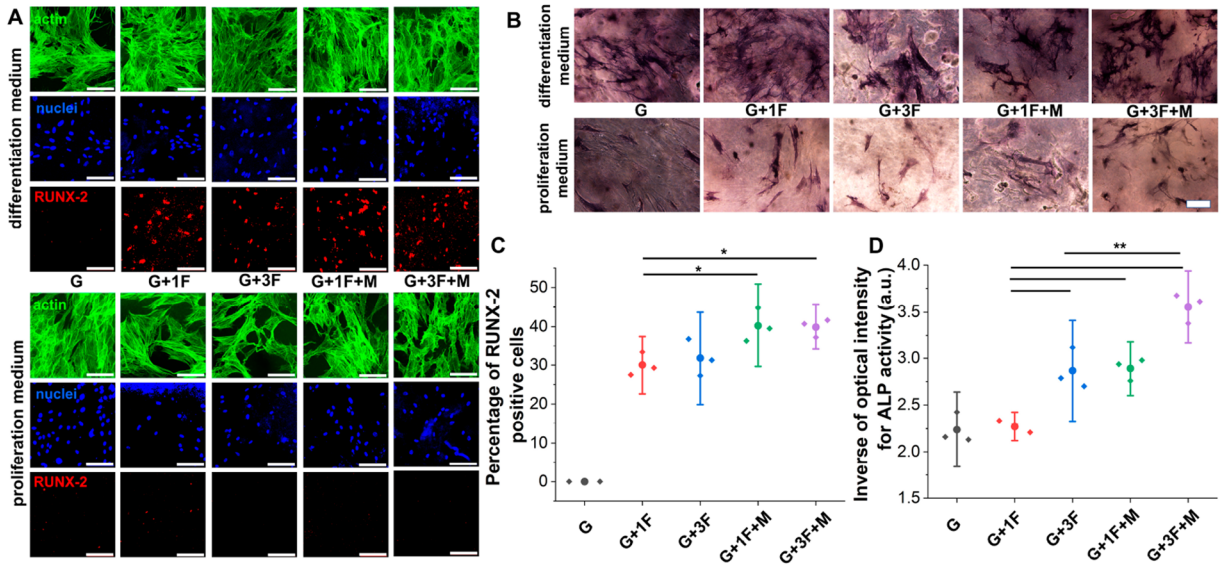

Figure 5. Comparison of ADSCs early stage osteogenic differentiation. (A) Representative confocal z-stack projection images (25 slices over 100 μm) of ADSC encapsulated in different hydrogel samples for 7 days; (B) representative bright-field microscope images of the inner surface of the hydrogels after staining with ALP when cultured in the presence of differentiation medium for 7 days; (C) percentage of RUNX-2 positive cells when cultured in the presence of differentiation medium for 7 days; and (D) inverse optical intensity of the ADSC-laden hydrogel outer surface, stained with ALP, when cultured in differentiation medium for 7 days (scale bar = 100 μm).

that the presence of magnetic nanofibers did not induce a cytotoxic environment for cell growth.

Next, the cells were fixed after 48 h and stained with phthalloidin (actin filaments) and DAPI (cell nuclei) to evaluate the changes in morphology caused by the presence of fibers and applied magnetic fields. The morphologies of ADSCs in different hydrogel samples were compared. As shown in Figure 4A, ADSCs exhibited a more elongated appearance in the G+1F and G+3F samples than in G. The presence of 1% and 3% nanofibers in the hydrogels resulted in a 22% and 59% increase in the number of stretched cells, respectively, compared to G, as depicted in Figure 4B. The average cell cytoplasm area (Figure 4C) also increased by 30% and 46%, respectively, while a similar trend was also observed for cell aspect ratio and roundness (Figure 4D, E). Notably, the storage moduli of the G+1F and G samples were comparable (Figure 3B), indicating that the presence of nanofibers in the system provided attachment sites for the encapsulated cells, leading to the observed increase in the number of stretched cells. These findings are consistent with previous reports by other researchers,[58,75] which suggest a positive relationship between the quantity of fiber loading and the degree of cell stretching.

The higher modulus of the G+3F samples (Figure 3B) had a significant effect on the number of stretched cells (Figure 4B), suggesting that the stiffness plays a role in the cellular morphology. When the G+3F samples were exposed to a static magnetic force, there was an 83% and 104% increase compared to G in the number of stretched cells and average cytoplasm area, respectively, were observed indicating the combined effects of stiffening through magnetic actuation and the presence of a nanofibrous environment. Interestingly, there was no change in the number of stretched cells or average cytoplasm surface area among the G samples with and without a magnetic field (Figure 4B, C), indicating that the magnetic field itself had no effect on the cell morphology. Magnetic rheology also proved that there was no effect of the magnetic field in the mechanical properties of the G samples. However, in the presence of a magnetic field, the stiffening of the G+3F samples resulted in 15% and 40% increases in the number of stretched cells and average cytoplasm surface area, respectively, compared to when there was no magnetic field (Figure 4B, C). These results suggest that both the fibrous network and stiffening through mechanical actuation play a role in guiding cell elongation. The presence of nanofibers in the G+3F samples may provide natural tissue-like complex architectures with improved adhesion cues, leading to the elongated and branched morphology of the cells. Additionally, the magnetic forces acting between the nanofibers and the cells has the potential to stimulate cell surface receptors, boosting cell adhesion and related activity.[76,77] The complementary effects of fiber content, organization/orientation, and stiffening are challenging to deconstruct and require further research.

3.3.4.2. Composite Hydrogels Stiffening Favors ADSC's Osteogenic Differentiation. After analyzing ADSC's morphometric changes in different hydrogel samples, we evaluated the differentiation potential of the cells after exposure to lineage guiding soluble supplements. As the increased cell surface area and decrease in cytoplasm roundness have previously been shown to correspond with osteogenic linage commitment in ADSC's,[78−80] we proposed that these morphometric changes will bias the cells toward osteogenesis. To test this, we exposed the hydrogel samples in both proliferation medium and osteogenic differentiation medium for up to 21 days. After 7 days of culture in proliferation and differentiation medium, hydrogel samples were fixed and stained with RUNX-2, a transcription factor that plays a crucial role in determining early stage osteogenic differentiation.[81,82] RUNX-2 guides mesenchymal stem cells toward preosteoblast differentiation while blocking their ability to differentiate into adipocytes and chondrocytes.[83]

Surprisingly, we did not detect any RUNX-2 expression in all G, G+1F and G+3F samples exposed to proliferation medium (Figure 5A). Also, we did not find any positive RUNX-2 expression in cells encapsulated within G samples exposed to osteo inductive medium (Figure 5C). However, we observed higher RUNX-2 expression in G+1F and G+3F samples (~30% and ~32%, respectively), with no significant difference between these two groups (Figure 5C). When we continuously exposed the gels to an external magnetic field, a further increase in RUNX-2 expression (~40% in both groups) was observed (Figure 5C). This increase may be due to the higher surface area of the cells (Figure 4C) found in the G+1F+M and G+3F+M samples when exposed to an external magnetic field, which leads to enhanced stiffness. Higher stiffness promotes cell-ECM interaction, increased tension within the cells, and the formation of a more mature cytoskeleton, which has been shown to trigger the expression of osteogenic genes, including RUNX-2.[74,84] Moreover, the nanofeatures from the incorporation of the nanofiber fragments is also expected to assist in coordinating osteogenic signal transduction.[85]

https://doi.org/10.1021/acsami.3c07021
ACS Appl. Mater. Interfaces XXXX, XXX, XXX−XXX

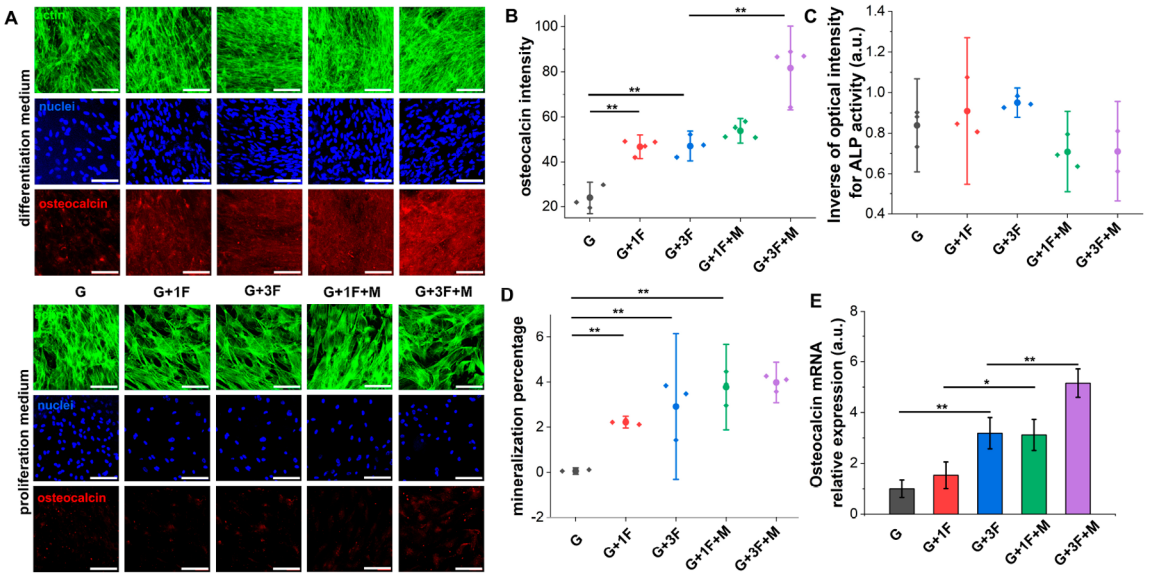

Figure 6. Comparison of ADSC late-stage osteogenic differentiation. (A) Representative confocal z-stack projection images (25 slices over 100 μm) of ADSC encapsulated in different hydrogel samples for 21 days, (B) intensity of osteocalcin expression across different samples when cultured with differentiation medium, (C) inverse optical intensity of the ADSC-laden hydrogel outer surface after being stained with ALP exposed into differentiation medium, (D) mineralization percentage found in the samples exposed into differentiation medium, and (E) normalized mRNA expression levels of osteocalcin in ADSCs after 21 days of exposure to the differentiation medium (scale bar = 100 μm).

To further support the immunofluorescence data, we stained the cells encapsulated in different hydrogel samples for alkaline phosphatase (ALP) after culture in proliferation and differentiation medium for 7 days (Figure 5B). ALP is an enzyme that osteoblasts express during bone formation and is a marker of early osteogenic differentiation.[86,87] We detect higher ALP activity in all G, G+1F and G+3F samples exposed to differentiation medium compared to proliferation medium (Figure 5B). For conditions without a magnetic field, cells encapsulated in the G+3F samples showed the highest ALP staining. However, when the fiber loaded gels were exposed to a continuous magnetic field, a consistent increase in stain intensity was noticed between G+1F+M and G+3F+M samples (Figure 5D). The magnetic field exposure led to approximately a 13% increase in the ALP intensity in both G+1F+M and G+3F+M samples. The similar trend between immunofluorescence and ALP activity assessment provides further evidence that these conditions are favorable for osteogenesis.

Having observed evidence to support osteogenic lineage specification at day 7, we next sought to verify osteogenesis at day 21 in these hydrogels. Osteocalcin is a protein that is produced by osteoblasts during bone formation and is considered a marker of late-stage osteogenic differentiation.[88,89] After 21 days of differentiation, all the G+1F, G+3F, G+1F+M, and G+3F+M samples exposed to osteogenic medium show significantly higher osteocalcin expression compared to the G samples (Figure 6B). This result indicates that the presence of fragmented nanofibers can significantly influence ADSC's osteogenic differentiation. Comparing the osteocalcin expression among the G +1F and G+1F+M samples, at day 21, there is no significant difference in expression with and without magnetic field exposure. However, there was an approximate 75% increase in osteocalcin expression in the G+3F+M samples compared to G+3F samples (Figure 6B). To supplement these results, we measured the mRNA expression levels of osteocalcin in samples exposed to differentiation medium and observed approximately 104% and 62% upregulation of osteocalcin transcript expression in the G+1F+M and G+3F+M samples, respectively, compared to the G+1F and G+3F samples (Figure 6E).

Interestingly, staining the late-stage osteogenic cultures with ALP indicated lower intensity in all the samples exposed to differentiation medium, when compared to day 7 samples. Literature suggests that ALP activity peaks during the early stages of bone formation and gradually recedes as mineralization takes place.[90,91] When comparing stain intensity across samples exposed to osteo inductive medium, no significant difference was observed. However, as differentiation continued, the samples became whitish and opaque due to mineralization (Supporting Figure 5A). To confirm that the developing opacity is due to deposited mineral phase, all the samples were scanned using a micro computed X-ray tomography (MicroCT) on day 21 and a Hounsfield value of 300 or higher was used to categorize the minerals developed in bones.[92] None of the samples exposed to proliferation medium or the G samples exposed to differentiation medium showed evidence of mineralization (Supporting Figure 5A). However, significantly higher mineralization was observed in all fiber loaded hydrogel samples. We found 70% higher mineralization in the G+1F+M samples compared to G+1F samples and 25% higher mineralization in the G+3F+M samples compared to G+3F samples. These findings demonstrate that stiffening through an external magnetic field influences osteogenic differentiation (Figure 6D).

Due to the mineralization, it is expected that the compressive stiffness of the gels would increase. To verify this, we measured the compressive modulus of the samples and found that G+1F+M and G +3F+M samples exposed to differentiation medium exhibit the highest Young's modulus (57 $\pm$ 7 and 66 $\pm$ 8 kPa, respectively) (Supporting Figure 5B). This represented an 80% and 81% increase in the G+1F+M and G+3F+M samples compared to the Young's modulus measured in the G+1F and G+3F samples exposed to differentiation medium (Supporting Figure 5B).

Based on all the analyses performed, it can be inferred that the addition of a small quantity of fiber fragments (1 wt/v%) can significantly impact the osteogenic differentiation of adipose-derived stem cells, without altering the initial substrate stiffness, suggesting the nanofibrous environment within the same stiffness range influences osteogenic differentiation. Moreover, the addition of a higher quantity of fiber fragments (3 wt/v%) can significantly alter the stiffness of a hydrogel, thus influencing osteogenic differentiation. Besides, the use of an external magnetic field to stiffen the substrate can further influence osteogenic differentiation. Thus, our study shows how a combination of a nanofibrous environment and substrate stiffening

https://doi.org/10.1021/acsami.3c07021
ACS Appl. Mater. Interfaces XXXX, XXX, XXX−XXX

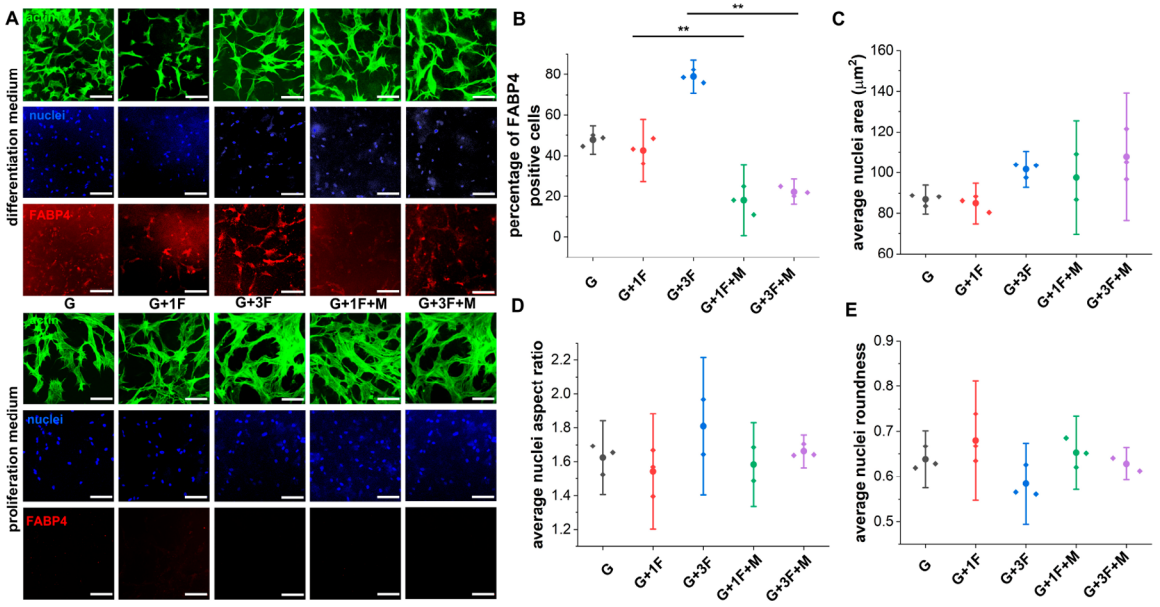

Figure 7. Morphology and fatty acid binding protein-4 expression analysis of ADSCs seeded in hydrogel (4% GelMa) and composite hydrogel samples for 7 days. (A) Representative confocal *z*-stack projection images (25 slices over 100 μm) of actin, nuclei, and FABP4 stained ADSCs seeded in different composite hydrogel samples over 7 days; (B) comparison of FABP4 positive cells across different hydrogel samples; (C) nuclear area for ADSCs in the different samples; (D) nuclear aspect ratio for cells in the different samples; and (E) nuclear roundness of the cells in the different samples (scale bar = 100 μm)

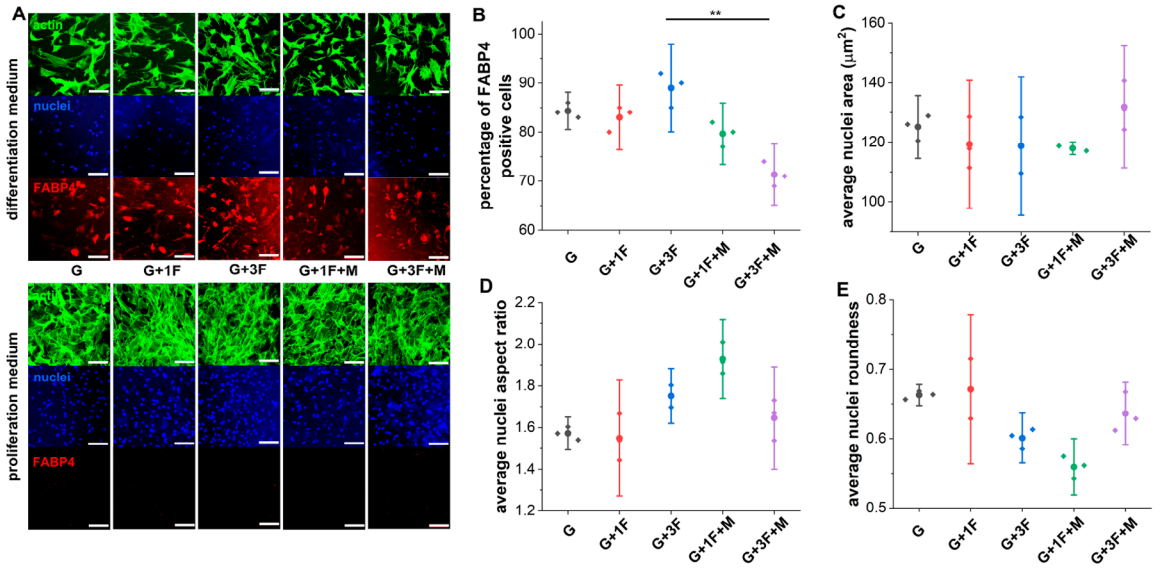

Figure 8. Comparison of ADSC's late-stage adipogenic differentiation after encapsulation in different hydrogel (4% GelMa) samples for 21 days. (A) Representative confocal z-stack projection images (25 slices over 100 μm) of actin, nuclei, and FABP4 stained ADSCs encapsulated in different hydrogel samples over 21 days; (B) plot for the percentage of positive FABP4 expressed cells across different samples while exposed to adipogenic differentiation medium; nuclear morphometric analysis plots of (C) average area, (D) aspect ratio, and (E) roundness of cells exposed to differentiation medium (scale bar = 100 μm).

can play a pronounced role in directing osteogenic differentiation of adipose-derived stem cells.

3.3.4.3. Nanofibrous Network and Matrix Stiffening Effects on Adipogenic Differentiation. After analyzing the impact of stiffening and a nanofibrous environment on the osteogenic differentiation of ADSCs, we proceeded to investigate how these factors affect the alternative lineage program adipogenesis. In contrast to the enhanced cytoskeletal tension and highly spread shape characteristics observed during osteogenesis, previous studies have suggested that a round morphology with low spreading is beneficial to adipogenic differentiation.[93−95] For this experiment, we optimized microenvironment conditions for adipogenic differentiation including (1) high seeding density (50 000 cells/mL) and (2) softer hydrogels (hydrogels made with 4% GelMa; 0.4 kPa stiffness). After 7 days of culture, all of the samples that were exposed to adipogenic inductive medium showed decreased cell spreading compared to those exposed to proliferation medium (Figure 7A). The adipogenic medium aids in the actin filaments reorganization toward the cell perimeter as the cell differentiation continues, resulted in smaller cytoplasm area.[96] ADSC's encapsulated in G+1F, G+3F, G+1F+M, and G+3F+M samples show slightly higher cytoplasm area, aspect ratio, and roundness (Supporting Figure 6A), although this result is not statistically significant. In addition to the cell area, McColloch et al. observed a correlation between nuclear morphology and adipo-

https://doi.org/10.1021/acsami.3c07021
ACS Appl. Mater. Interfaces XXXX, XXX, XXX−XXX

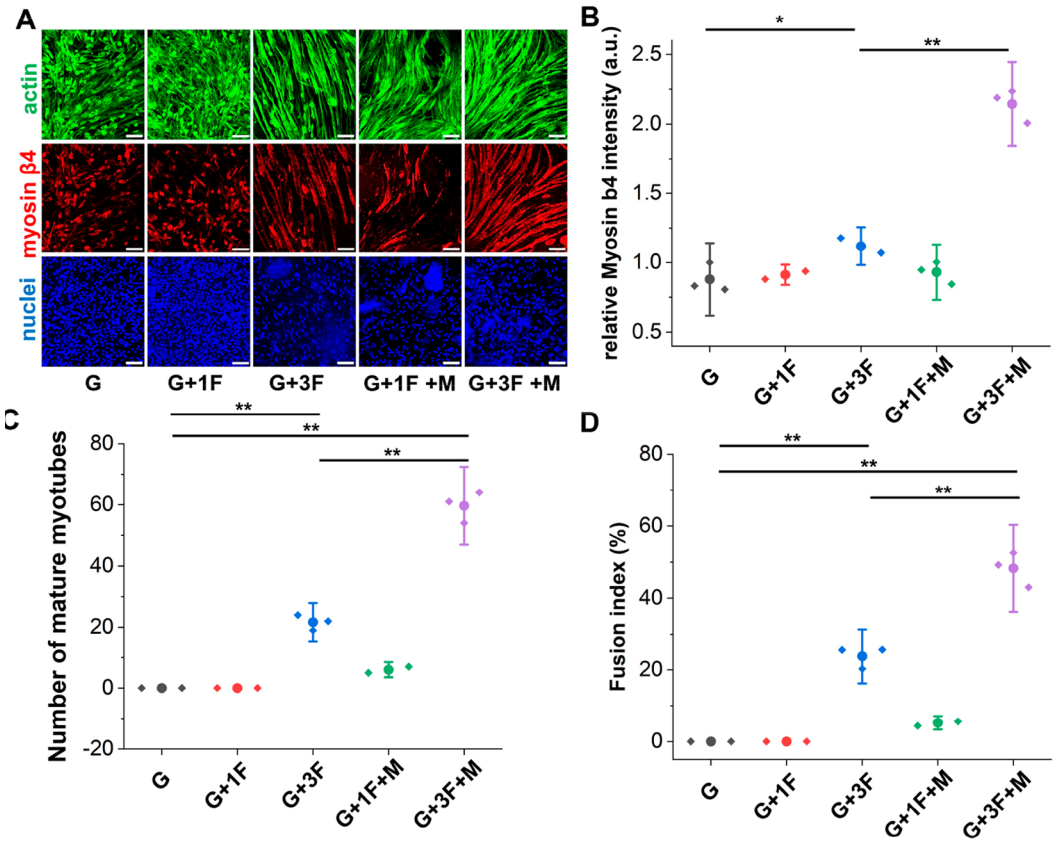

Figure 9. Comparison of C2C12's myogenic differentiation in different samples. (A) Representative confocal z-stack projection images (25 slices over 100 μm) of actin, myosin β4, and nuclei stained C2C12 encapsulated in different composite hydrogel samples over 7 days; (B) average myosin β4 intensity, (C) number of mature myotubes, and (D) fusion index (%) across different samples (scale bar = 100 μm).

genesis.[93] Here we observed a similar trend in nuclear morphology (average nuclei area, aspect ratio, and roundness) after exposure to adipo-inductive medium that is suggestive of differentiation (Figure 7C–E).

While morphometrics analysis is suggestive of differentiation, we performed immunofluorescence analysis for the fatty acid binding protein-4 (FABP4), which is predominantly expressed in cells undergoing adipogenesis.[97] Since this is a late-stage adipogenic protein expression marker, it was expected that the expression of FABP4 would be low at early time points.[98,99] Surprisingly, while there was low FABP4 expression in most conditions (<50%; Figure 7B), 80% of cells in G+3F samples (Figure 7B) exhibited FABP4 expression within 7 days, indicating that the nanofibrous environment might impart favorable cues for adipogenesis. We speculate that our nanofibers could mimic the collagen type I bundles found in the extracellular matrix of adipose tissue,[100,101] assisting in faster accumulation of lipid droplets. However, the G+1F+M and G+3F +M samples were exposed to a magnetic field, there was a considerable reduction of FABP4 expression, presumably due to stiffening,[102] response that promotes a spread cell morphology (Figure 7C).

Next, we evaluated the morphometrics of cells undergoing adipogenesis on day 21. There were no notable differences in nuclear (Figure 8C–E) and cytoplasm (Supporting Figure 6B) morphology between cells exposed to proliferation or differentiation conditions. However, we did observe a slight decrease in the average nuclear size of cells in the G, G+1F, and G+3F samples compared to day 7 when exposed to differentiation medium. This is likely because the actin stress fibers of the cells exert tension on the nuclear membrane, helping to maintain its shape. As the cells undergo differentiation and the actin filaments are reorganized, this tension is released, leading to morphological changes in the nucleus. Additionally, the formation of lipid droplets during this process exerts a further force on the nucleus. Previous research has shown that as lipid droplets accumulate during adipogenesis, actin tension decreases over time.[93] Despite these changes, we did not find any significant differences in the aspect ratio or roundness of the nuclei or cytoplasm among the samples exposed to the adipogenic differentiation medium at day 21 compared to day 7. Comparing the average cytoplasm area of the cells exposed to differentiation medium at day 7 and day 21, no significant difference was detected.

Immunofluorescence characterization of FABP4 expression at day 21 indicates a similar trend of increased expression with fiber content observed in the day 7 experiments, followed by decreased expression upon stiffening with a magnetic field. Cells grew in the G+3F samples, without the magnetic actuation, show the highest, and with the magnetic field actuation in G+3F+M samples, show the lowest FABP4 expression (Figure 8B). Transcript analysis of PPARγ mRNA supports this result (Supporting Figure 7C).

To support the molecular marker results, we conducted Oil-Red-O staining to quantify the formation of lipid droplets, an important composition in cells undergoing adipogenesis. We captured images from different focus points in bright fields to ensure that the entire gel sample was included. The results showed that the G+3F samples had the highest number of lipid droplets (Supporting Figure 7B), consistent with the immunofluorescence analysis (Figure 8B). Taken together, these results show how softness and a nanofibrous microenvironment are advantageous to cells undergoing adipogenesis. In contrast, stiffening through applied magnetic fields encourages cell spreading, which obviates adipogenic lineage specification.

3.3.5. Stiffening Influences Morphogenesis of Embryonic Skeletal Muscle Cells. Platforms that can steer differentiation outcome with an external trigger will have broad utility in cell and tissue engineering. Another potential avenue for the use of dynamic

https://doi.org/10.1021/acsami.3c07021
ACS Appl. Mater. Interfaces XXXX, XXX, XXX−XXX

stiffening matrices is in coaxing morphogenesis. Having demonstrated some control in guiding the differentiation of ADSCs toward osteogenic and adipogenic linage, we next explored the ability of fiber loaded gels to guide active morphogenesis processes like skeletal muscle formation.

Engineering functional muscle tissue *in vitro* remains a difficult task due to structural complexity. Current challenges include: (1) myotube formation and 3D tissue mimicry-organization into tightly packed and aligned structures and (2) achieving advanced maturation of the myotubes through the formation and development of sarcomeres.[103] Embryonic muscle cells, specifically those of the C2C12 lineage is an extensively used cell line to study the effect of mechanical stimuli of the substrate into myoblast differentiation.[104,105] While there have been reports of ADSCs undergoing skeletal myogenesis with select media supplements,[106] the C2C12 is a more robust cell type that is widely used for demonstrating muscle differentiation. C2C12 cells can be differentiated easily in culture by replacing fetal bovine serum (FBS) with horse serum in their culture medium.[107] This method of maturation has been extensively studied in the literature and is the preferred method for developing prototype skeletal muscle tissue. Typically, these cells take 7 days to develop contractions in the presence of horse serum and can be identified by multinuclear formation and the expression of myosin 4.[108]

Numerous studies have demonstrated that C2C12 differentiation and maturation can be influenced by controlling the stiffness of the substrate and applying external stimuli, even in the absence of differentiation medium.[107,109,110] It has also been reported that C2C12's best myogenic differentiation is achieved in the substrate stiffness in the range of 1−6 kPa.[103,111] Therefore, we used 6% GelMa (3.5 kPa, Supporting Figure 8A) as a control gel for these experiments. We encapsulated 50 000 cells/mL into the control and fiber loaded gels in the presence of typical proliferation medium and let the cultures proceed for 7 days.

After 7 days almost all the C2C12 cells encapsulated in G and G +1F samples had rounded morphology. However, in the G+3F and G +3F+M samples, the cells exhibited a highly elongated morphology (Figure 9A). During muscle differentiation, a multinucleated cell containing three of more nuclei is considered a myotube.[112,113] None of the G and G+1F samples had any myotubes present (Figure 9A, C). However, the G+3F samples had substantially higher number of myotubes (Figure 9C) and fusion index (Figure 9D). This number increased (Figure 9C, D) 172% in the G+3F+M samples, indicating that magnetic strain not only induces myogenic differentiation but also promotes a mature skeletal muscle phenotype.

Next, we evaluated the maturation status of these prototype myotubes through the immunofluorescence characterization of myosin β4 expression (Figure 9B). Compared with G samples, we observed a 28% increase in myosin β4 expression in the G+3F samples (Figure 9B), indicating that the fiber loaded hydrogels alone can trigger C2C12 myogenesis. Previous studies have shown that nanofibers can influence C2C12 cell differentiation in 2D, and the presence of a nanofibrous environment in 3D can thus be claimed to resemble the natural extracellular matrix (ECM), facilitating C2C12 differentiation.[114,115] We observed a 93% increase in the myosin β4 expression (Figure 9B) in G+3F+M samples compared to G+3F samples, thereby indicative that stiffening can further influence C2C12's myogenic differentiation. Our result is consistent with a previous report that demonstrated enhanced C2C12 myogenesis in magnetic nanoparticle-laden hydrogels subjected to stiffening.[116] Overall, we reason that magnetic field induces strain within the hydrogel through movement of the nanofibers in response to the field, which will accommodate cell migration, alignment, and fusion inside the gels, thereby enhancing cell-matrix interactions to direct skeletal myogenesis.[117]

3.4. Conclusion. In this paper, we describe the synthesis process for creating fiber-loaded hydrogels that respond to external magnetic stimulation. We investigated the influence of the fiber loading density and magnetic actuation on the mechanical properties of the hydrogels. Magnetic rheological measurements indicated that magnetic fields successfully induced stiffening in the hydrogels. These fiber-loaded gels showed great potential in controlling adipose derived stem cell (ADSC) differentiation toward different lineages depending on static stiffness and nanofibrous morphology, which could be modulated by attenuation of a magnetic field. The presence of fibers promoted both adipogenesis and osteogenesis: 3% fiber loaded hydrogels without stiffening (G+3F) were optimal for adipogenesis, and 3% fiber loaded hydrogels with stiffening (G+3F+M) were optimal for osteogenesis. We explored the versatility of these fiber loaded hydrogels in muscle tissue generation and found that the magnetic field influences myogenic differentiation and maturation of C2C12 cells with the 3% fiber hydrogels with stiffening leading to enhanced fusion and expression of molecular markers of maturation. Our findings indicate that this stimuli-responsive fiber-loaded hydrogel system has the potential to be a useful platform for studies of fundamental cellular processes and for aiding the engineering of tissue for regenerative medicine.

■ ASSOCIATED CONTENT

Supporting Information

The Supporting Information is available free of charge at https://pubs.acs.org/doi/10.1021/acsami.3c07021.

FTIR spectra of synthesized and cross-linked nanofiber, EDS mapping of nanofiber loaded hydrogels, the magnetic characterization of the magnetic nanofiber loaded hydrogel samples using a vibrating sample magnetometer at 300 K, live−dead analysis of ADSC-loaded hydrogel samples, microCT analysis heatmap of the density of microgel matrices after being exposed to osteogenic medium for 21 days, morphometric analysis of encapsulated ADSC in different hydrogel samples when exposed to adipogenic differentiation medium, quantification of the number of mature lipid droplets present in the hydrogel samples when exposed to adipogenic differentiation medium, rheological analysis of fiber loaded hydrogels made with 6% GelMa, and representative ALP-stained images of different hydrogel samples (PDF)

■ AUTHOR INFORMATION

Corresponding Author

Kristopher A. Kilian − *School of Materials Science and Engineering, University of New South Wales (UNSW Sydney), Sydney, New South Wales 2052, Australia; School of Chemistry, Australian Centre for NanoMedicine, University of New South Wales (UNSW Sydney), Sydney, New South Wales 2052, Australia;* orcid.org/0000-0002-8963-9796; Email: k.kilian@unsw.edu.au

Authors

Md Shariful Islam − *School of Materials Science and Engineering, University of New South Wales (UNSW Sydney), Sydney, New South Wales 2052, Australia*

Thomas G. Molley − *School of Materials Science and Engineering, University of New South Wales (UNSW Sydney), Sydney, New South Wales 2052, Australia*

Tzong-tyng Hung − *Biological Resources Imaging Laboratory, Mark Wainwright Analytical Centre, University of New South Wales (UNSW Sydney), Sydney, New South Wales 2052, Australia*

C. I. Sathish − *School of Engineering, College of Engineering, Science and Environment, The University of Newcastle, Callaghan, New South Wales 2308, Australia*

https://doi.org/10.1021/acsami.3c07021
ACS Appl. Mater. Interfaces XXXX, XXX, XXX−XXX

Vina D. L. Putra − *School of Materials Science and Engineering, University of New South Wales (UNSW Sydney), Sydney, New South Wales 2052, Australia*
Gagan K. Jalandhra − *School of Materials Science and Engineering, University of New South Wales (UNSW Sydney), Sydney, New South Wales 2052, Australia*
Jake Ireland − *School of Chemistry, Australian Centre for NanoMedicine, University of New South Wales (UNSW Sydney), Sydney, New South Wales 2052, Australia*
Yancheng Li − *School of Civil and Environmental Engineering, University of Technology Sydney, Sydney, New South Wales 2007, Australia*
Jiabao Yi − *School of Engineering, College of Engineering, Science and Environment, The University of Newcastle, Callaghan, New South Wales 2308, Australia;* orcid.org/0000-0001-5299-9897
Jamie J. Kruzic − *School of Mechanical and Manufacturing Engineering, University of New South Wales (UNSW Sydney), Sydney, New South Wales 2052, Australia*

Complete contact information is available at: https://pubs.acs.org/10.1021/acsami.3c07021

Notes

The authors declare no competing financial interest.

■ ACKNOWLEDGMENTS

This work was supported through funding from the National Health and Medical Research Council (K.A.K.: APP1185021), the Australian Research Council (K.A.K. & J.J.K: DP210103654), and the National Cancer Institute of the National Institutes of Health (K.A.K.: R01CA251443). The authors acknowledge the help and support of staff from the Electron microscope unit, Biomedical Imaging Facility, and the Biological Specimen Preparation Laboratory of the UNSW Mark Wainwright Analytical Center.

■ REFERENCES

(1) Elangwe, C. N.; Morozkina, S. N.; Olekhnovich, R. O.; Polyakova, V. O.; Krasichkov, A.; Yablonskiy, P. K.; Uspenskaya, M. V. Pullulan-Based Hydrogels in Wound Healing and Skin Tissue Engineering Applications: A Review. *International Journal of Molecular Sciences* **2023**, *24* (5), 4962.
(2) Pramanik, S.; Kharche, S.; More, N.; Ranglani, D.; Singh, G.; Kapusetti, G. Natural Biopolymers for Bone Tissue Engineering: A Brief Review. *Engineered Regeneration* **2023**, *4* (2), 193−204.
(3) Lu, T.; Li, Y.; Chen, T. Techniques for Fabrication and Construction of Three-Dimensional Scaffolds for Tissue Engineering. *International journal of nanomedicine* **2013**, 337−350.
(4) Shapiro, J. M.; Oyen, M. L. Hydrogel Composite Materials for Tissue Engineering Scaffolds. *Jom* **2013**, *65*, 505−516.
(5) Guo, Y.; Du, S.; Quan, S.; Jiang, F.; Yang, C.; Li, J. Effects of Biophysical Cues of 3d Hydrogels on Mesenchymal Stem Cells Differentiation. *Journal of Cellular Physiology* **2021**, *236* (4), 2268−2275.
(6) Musah, S.; Wrighton, P. J.; Zaltsman, Y.; Zhong, X.; Zorn, S.; Parlato, M. B.; Hsiao, C.; Palecek, S. P.; Chang, Q.; Murphy, W. L.; Kiessling, L. L. Substratum-Induced Differentiation of Human Pluripotent Stem Cells Reveals the Coactivator Yap Is a Potent Regulator of Neuronal Specification. *Proc. Natl. Acad. Sci. U. S. A.* **2014**, *111* (38), 13805−13810.
(7) Bosworth, L. A.; Turner, L.-A.; Cartmell, S. H. State of the Art Composites Comprising Electrospun Fibres Coupled with Hydrogels: A Review. *Nanomedicine: Nanotechnology, Biology and Medicine* **2013**, *9* (3), 322−335.
(8) Kumar, A.; Placone, J. K.; Engler, A. J. Understanding the Extracellular Forces That Determine Cell Fate and Maintenance. *Development* **2017**, *144* (23), 4261−4270.
(9) Hoffman, A. S. Hydrogels for Biomedical Applications. *Advanced drug delivery reviews* **2012**, *64*, 18−23.
(10) Taneja, H.; Salodkar, S. M.; Singh Parmar, A.; Chaudhary, S. Hydrogel Based 3d Printing: Bio Ink for Tissue Engineering. *J. Mol. Liq.* **2022**, *367*, 120390.
(11) Fang, W.; Yang, M.; Wang, L.; Li, W.; Liu, M.; Jin, Y.; Wang, Y.; Yang, R.; Wang, Y.; Zhang, K.; Fu, Q. Hydrogels for 3d Bioprinting in Tissue Engineering and Regenerative Medicine: Current Progress and Challenges. *International Journal of Bioprinting* **2023**, *9* (5), 759.
(12) Rose, J. C.; De Laporte, L. Hierarchical Design of Tissue Regenerative Constructs. *Adv. Healthcare Mater.* **2018**, *7* (6), 1701067.
(13) Chen, Y.; Hao, Y.; Mensah, A.; Lv, P.; Wei, Q. Bio-Inspired Hydrogels with Fibrous Structure: A Review on Design and Biomedical Applications. *Biomaterials Advances* **2022**, *136*, 212799.
(14) Khuu, N.; Kheiri, S.; Kumacheva, E. Structurally Anisotropic Hydrogels for Tissue Engineering. *Trends in Chemistry* **2021**, *3* (12), 1002−1026.
(15) Tan, G. Z.; Zhou, Y. Electrospinning of Biomimetic Fibrous Scaffolds for Tissue Engineering: A Review. *International Journal of Polymeric Materials and Polymeric Biomaterials* **2020**, *69* (15), 947−960.
(16) Butcher, A. L.; Offeddu, G. S.; Oyen, M. L. Nanofibrous Hydrogel Composites as Mechanically Robust Tissue Engineering Scaffolds. *Trends Biotechnol.* **2014**, *32* (11), 564−570.
(17) Yang, Y.; Wimpenny, I.; Ahearne, M. Portable Nanofiber Meshes Dictate Cell Orientation Throughout Three-Dimensional Hydrogels. *Nanomedicine: Nanotechnology, Biology and Medicine* **2011**, *7* (2), 131−136.
(18) Cui, Z.; Wright, L. D.; Guzzo, R.; Freeman, J. W.; Drissi, H.; Nair, L. S. Poly (D-Lactide)/Poly (Caprolactone) Nanofiber-Thermogelling Chitosan Gel Composite Scaffolds for Osteochondral Tissue Regeneration in a Rat Model. *J. Bioact. Compat. Polym.* **2013**, *28* (2), 115−125.
(19) Tonsomboon, K.; Oyen, M. L. Composite Electrospun Gelatin Fiber-Alginate Gel Scaffolds for Mechanically Robust Tissue Engineered Cornea. *Journal of the mechanical behavior of biomedical materials* **2013**, *21*, 185−194.
(20) Hsieh, A.; Zahir, T.; Lapitsky, Y.; Amsden, B.; Wan, W.; Shoichet, M. S. Hydrogel/Electrospun Fiber Composites Influence Neural Stem/Progenitor Cell Fate. *Soft Matter* **2010**, *6* (10), 2227−2237.
(21) Caliari, S. R.; Harley, B. A. The Effect of Anisotropic Collagen-Gag Scaffolds and Growth Factor Supplementation on Tendon Cell Recruitment, Alignment, and Metabolic Activity. *Biomaterials* **2011**, *32* (23), 5330−5340.
(22) Ghaderinejad, P.; Najmoddin, N.; Bagher, Z.; Saeed, M.; Karimi, S.; Simorgh, S.; Pezeshki-Modaress, M. An Injectable Anisotropic Alginate Hydrogel Containing Oriented Fibers for Nerve Tissue Engineering. *Chem. Eng. J.* **2021**, *420*, 130465.
(23) Saunders, L.; Ma, P. X. Self-Healing Supramolecular Hydrogels for Tissue Engineering Applications. *Macromol. Biosci.* **2019**, *19* (1), 1800313.
(24) Ruskowitz, E. R.; DeForest, C. A. Photoresponsive Biomaterials for Targeted Drug Delivery and 4d Cell Culture. *Nat. Rev. Mater.* **2018**, *3* (2), 1−17.
(25) El-Husseiny, H. M.; Mady, E. A.; Hamabe, L.; Abugomaa, A.; Shimada, K.; Yoshida, T.; Tanaka, T.; Yokoi, A.; Elbadawy, M.; Tanaka, R. Smart/Stimuli-Responsive Hydrogels: Cutting-Edge Platforms for Tissue Engineering and Other Biomedical Applications. *Materials Today Bio* **2022**, *13*, 100186.
(26) Lavanya, K.; Chandran, S. V.; Balagangadharan, K.; Selvamurugan, N. Temperature-and Ph-Responsive Chitosan-Based Injectable Hydrogels for Bone Tissue Engineering. *Materials Science and Engineering: C* **2020**, *111*, 110862.

(27) Kim, Y.; Hu, Y.; Jeong, J.-p.; Jung, S. Injectable, Self-Healable and Adhesive Hydrogels Using Oxidized Succinoglycan/Chitosan for Ph-Responsive Drug Delivery. *Carbohydr. Polym.* **2022**, *284*, 119195.
(28) Klouda, L. Thermoresponsive Hydrogels in Biomedical Applications: A Seven-Year Update. *Eur. J. Pharm. Biopharm.* **2015**, *97*, 338−349.
(29) Miguel, S. P.; Ribeiro, M. P.; Brancal, H.; Coutinho, P.; Correia, I. J. Thermoresponsive Chitosan-Agarose Hydrogel for Skin Regeneration. *Carbohydr. Polym.* **2014**, *111*, 366−373.
(30) Nie, L.; Li, J.; Lu, G.; Wei, X.; Deng, Y.; Liu, S.; Zhong, S.; Shi, Q.; Hou, R.; Sun, Y.; et al. Temperature Responsive Hydrogel for Cells Encapsulation Based on Graphene Oxide Reinforced Poly (N-Isopropylacrylamide)/Hydroxyethyl-Chitosan. *Mater. Today Commun.* **2022**, *31*, 103697.
(31) Liu, Z.; Liu, J.; Cui, X.; Wang, X.; Zhang, L.; Tang, P. Recent Advances on Magnetic Sensitive Hydrogels in Tissue Engineering. *Frontiers in chemistry* **2020**, *8*, 124.
(32) Pardo, A.; Gómez-Florit, M.; Barbosa, S.; Taboada, P.; Domingues, R. M.; Gomes, M. E. Magnetic Nanocomposite Hydrogels for Tissue Engineering: Design Concepts and Remote Actuation Strategies to Control Cell Fate. *ACS Nano* **2021**, *15* (1), 175−209.
(33) Braunmiller, D. L.; Babu, S.; Gehlen, D. B.; Seuß, M.; Haraszti, T.; Falkenstein, A.; Eigen, J.; De Laporte, L.; Crassous, J. J. Pre-Programmed Rod-Shaped Microgels to Create Multi-Directional Anisogels for 3d Tissue Engineering. *Adv. Funct. Mater.* **2022**, *32* (50), 2202430.
(34) Li, Z.; Li, Y.; Chen, C.; Cheng, Y. Magnetic-Responsive Hydrogels: From Strategic Design to Biomedical Applications. *J. Controlled Release* **2021**, *335*, 541−556.
(35) Seo, J. Y.; Park, S. B.; Kim, S. Y.; Seo, G. J.; Jang, H.-K.; Lee, T.-J. Acoustic and Magnetic Stimuli-Based Three-Dimensional Cell Culture Platform for Tissue Engineering. *Tissue Engineering and Regenerative Medicine* **2023**, *20*, 563.
(36) Pardo, A.; Bakht, S. M.; Gomez-Florit, M.; Rial, R.; Monteiro, R. F.; Teixeira, S. P.; Taboada, P.; Reis, R. L.; Domingues, R. M.; Gomes, M. E. Magnetically-Assisted 3d Bioprinting of Anisotropic Tissue-Mimetic Constructs. *Adv. Funct. Mater.* **2022**, *32* (50), 2208940.
(37) Yue, B. Biology of the Extracellular Matrix: An Overview. *Journal of glaucoma* **2014**, *23*, S20.
(38) Karimi, S.; Bagher, Z.; Najmoddin, N.; Simorgh, S.; Pezeshki-Modaress, M. Alginate-Magnetic Short Nanofibers 3d Composite Hydrogel Enhances the Encapsulated Human Olfactory Mucosa Stem Cells Bioactivity for Potential Nerve Regeneration Application. *Int. J. Biol. Macromol.* **2021**, *167*, 796−806.
(39) Hiraki, H. L.; Matera, D. L.; Rose, M. J.; Kent, R. N.; Todd, C. W.; Stout, M. E.; Wank, A. E.; Schiavone, M. C.; DePalma, S. J.; Zarouk, A. A.; Baker, B. M. Magnetic Alignment of Electrospun Fiber Segments within a Hydrogel Composite Guides Cell Spreading and Migration Phenotype Switching. *Frontiers in Bioengineering and Biotechnology* **2021**, *9*, 679165.
(40) Wang, L.; Li, T.; Wang, Z.; Hou, J.; Liu, S.; Yang, Q.; Yu, L.; Guo, W.; Wang, Y.; Guo, B.; et al. Injectable Remote Magnetic Nanofiber/Hydrogel Multiscale Scaffold for Functional Anisotropic Skeletal Muscle Regeneration. *Biomaterials* **2022**, *285*, 121537.
(41) Li, Y.; Huang, G.; Zhang, X.; Li, B.; Chen, Y.; Lu, T.; Lu, T. J.; Xu, F. Magnetic Hydrogels and Their Potential Biomedical Applications. *Adv. Funct. Mater.* **2013**, *23* (6), 660−672.
(42) Abdeen, A. A.; Lee, J.; Bharadwaj, N. A.; Ewoldt, R. H.; Kilian, K. A. Temporal Modulation of Stem Cell Activity Using Magneto-active Hydrogels. *Adv. Healthcare Mater.* **2016**, *5* (19), 2536−2544.
(43) Jiang, Q.; Reddy, N.; Yang, Y. Cytocompatible Cross-Linking of Electrospun Zein Fibers for the Development of Water-Stable Tissue Engineering Scaffolds. *Acta biomaterialia* **2010**, *6* (10), 4042−4051.
(44) Jiang, Q.; Xu, H.; Cai, S.; Yang, Y. Ultrafine Fibrous Gelatin Scaffolds with Deep Cell Infiltration Mimicking 3d Ecms for Soft Tissue Repair. *J. Mater. Sci.: Mater. Med.* **2014**, *25*, 1789−1800.
(45) Loessner, D.; Meinert, C.; Kaemmerer, E.; Martine, L. C.; Yue, K.; Levett, P. A.; Klein, T. J.; Melchels, F. P.; Khademhosseini, A.; Hutmacher, D. W. Functionalization, Preparation and Use of Cell-Laden Gelatin Methacryloyl-Based Hydrogels as Modular Tissue Culture Platforms. *Nature protocols* **2016**, *11* (4), 727−746.
(46) Susaki, E. A.; Tainaka, K.; Perrin, D.; Kishino, F.; Tawara, T.; Watanabe, T. M.; Yokoyama, C.; Onoe, H.; Eguchi, M.; Yamaguchi, S.; et al. Whole-Brain Imaging with Single-Cell Resolution Using Chemical Cocktails and Computational Analysis. *Cell* **2014**, *157* (3), 726−739.
(47) Corbari, L.; Cambon-Bonavita, M.-A.; Long, G. J.; Grandjean, F.; Zbinden, M.; Gaill, F.; Compère, P. Iron Oxide Deposits Associated with the Ectosymbiotic Bacteria in the Hydrothermal Vent Shrimp Rimicaris Exoculata. *Biogeosciences* **2008**, *5* (5), 1295−1310.
(48) Cumming, M. H.; Leonard, A. R.; LeCorre-Bordes, D. S.; Hofman, K. Intra-Fibrillar Citric Acid Crosslinking of Marine Collagen Electrospun Nanofibres. *Int. J. Biol. Macromol.* **2018**, *114*, 874−881.
(49) Liguori, A.; Uranga, J.; Panzavolta, S.; Guerrero, P.; de la Caba, K.; Focarete, M. L. Electrospinning of Fish Gelatin Solution Containing Citric Acid: An Environmentally Friendly Approach to Prepare Crosslinked Gelatin Fibers. *Materials* **2019**, *12* (17), 2808.
(50) Uranga, J.; Leceta, I.; Etxabide, A.; Guerrero, P.; De La Caba, K. Cross-Linking of Fish Gelatins to Develop Sustainable Films with Enhanced Properties. *Eur. Polym. J.* **2016**, *78*, 82−90.
(51) Lee, D. H.; Arisaka, Y.; Tonegawa, A.; Kang, T. W.; Tamura, A.; Yui, N. Cellular Orientation on Repeatedly Stretching Gelatin Hydrogels with Supramolecular Cross-Linkers. *Polymers* **2019**, *11* (12), 2095.
(52) Baniasadi, H.; Ramazani S.A., A.; Mashayekhan, S. Fabrication and Characterization of Conductive Chitosan/Gelatin-Based Scaffolds for Nerve Tissue Engineering. *Int. J. Biol. Macromol.* **2015**, *74*, 360−366.
(53) Uranga, J.; Nguyen, B. T.; Si, T. T.; Guerrero, P.; de la Caba, K. The Effect of Cross-Linking with Citric Acid on the Properties of Agar/Fish Gelatin Films. *Polymers* **2020**, *12* (2), 291.
(54) Xu, H.; Shen, L.; Xu, L.; Yang, Y. Low-Temperature Crosslinking of Proteins Using Non-Toxic Citric Acid in Neutral Aqueous Medium: Mechanism and Kinetic Study. *Industrial Crops and Products* **2015**, *74*, 234−240.
(55) Nazemi, M. M.; Khodabandeh, A.; Hadjizadeh, A. Near-Field Electrospinning: Crucial Parameters, Challenges, and Applications. *ACS Appl. Bio Mater.* **2022**, *5* (2), 394−412.
(56) Ryu, H. I.; Koo, M. S.; Kim, S.; Kim, S.; Park, Y.-A.; Park, S. M. Uniform-Thickness Electrospun Nanofiber Mat Production System Based on Real-Time Thickness Measurement. *Sci. Rep.* **2020**, *10* (1), 20847.
(57) Kim, S.; Cha, C. Enhanced Mechanical and Electrical Properties of Heteroscaled Hydrogels Infused with Aqueous-Dispersible Hybrid Nanofibers. *Biofabrication* **2020**, *12* (1), 015020.
(58) Lee, S.; Kim, H. S.; Yoo, H. S. Electrospun Nanofibrils Embedded Hydrogel Composites for Cell Cultivation in a Biomimetic Environment. *RSC Adv.* **2017**, *7* (85), 54246−54253.
(59) Saeedi Garakani, S.; Khanmohammadi, M.; Atoufi, Z.; Kamrava, S. K.; Setayeshmehr, M.; Alizadeh, R.; Faghihi, F.; Bagher, Z.; Davachi, S. M.; Abbaspourrad, A. Fabrication of Chitosan/Agarose Scaffolds Containing Extracellular Matrix for Tissue Engineering Applications. *Int. J. Biol. Macromol.* **2020**, *143*, 533−545.
(60) Baniasadi, M.; Minary-Jolandan, M. Alginate-Collagen Fibril Composite Hydrogel. *Materials* **2015**, *8* (2), 799−814.
(61) Katiyar, A.; Dhar, P.; Das, S. K.; Nandi, T. Near-Field Magnetostatics and Néel-Brownian Interactions Mediated Magneto-Rheological Characteristics of Highly Stable Nano-Ferrocolloids. *Soft Matter* **2015**, *11* (8), 1614−1627.
(62) Pardo, A.; Pujales, R.; Blanco, M.; Villar-Alvarez, E. M.; Barbosa, S.; Taboada, P.; Mosquera, V. Analysis of the Influence of Synthetic Paramaters on the Structure and Physico-Chemical

https://doi.org/10.1021/acsami.3c07021
ACS Appl. Mater. Interfaces XXXX, XXX, XXX−XXX

Properties of Non-Spherical Iron Oxide Nanocrystals and Their Biological Stability and Compatibility. *Dalton Transactions* **2016**, *45* (2), 797−810.
(63) Pardo, A.; Yanez, S.; Pineiro, Y.; Iglesias-Rey, R.; Al-Modlej, A.; Barbosa, S.; Rivas, J.; Taboada, P. Cubic Anisotropic Co-and Zn-Substituted Ferrite Nanoparticles as Multimodal Magnetic Agents. *ACS Appl. Mater. Interfaces* **2020**, *12* (8), 9017−9031.
(64) Skubis, A.; Sikora, B.; Zmarzły, N.; Wojdas, E.; Mazurek, U. Adipose-Derived Stem Cells: A Review of Osteogenesis Differentiation. *Acta Universitatis Lodziensis. Folia Biologica et Oecologica* **2016**, *12*, 38−47.
(65) Guo, L.; Fan, Y.; Kawazoe, N.; Fan, H.; Zhang, X.; Chen, G. Fabrication of Gelatin-Micropatterned Surface and Its Effect on Osteogenic Differentiation of Hmscs. *J. Mater. Chem. B* **2018**, *6* (7), 1018−1025.
(66) Romanazzo, S.; Molley, T. G.; Nemec, S.; Lin, K.; Sheikh, R.; Gooding, J. J.; Wan, B.; Li, Q.; Kilian, K. A.; Roohani, I. Synthetic Bone-Like Structures through Omnidirectional Ceramic Bioprinting in Cell Suspensions. *Adv. Funct. Mater.* **2021**, *31* (13), 2008216.
(67) Bränmark, C.; Paul, A.; Ribeiro, D.; Magnusson, B.; Brolén, G.; Enejder, A.; Forslöw, A. Increased Adipogenesis of Human Adipose-Derived Stem Cells on Polycaprolactone Fiber Matrices. *PLoS One* **2014**, *9* (11), No. e113620.
(68) Qu, R.; He, K.; Yang, Y.; Fan, T.; Sun, B.; Khan, A. U.; Huang, W.; Ouyang, J.; Pan, X.; Dai, J. The Role of Serum Amyloid A1 in the Adipogenic Differentiation of Human Adipose-Derived Stem Cells Basing on Single-Cell Rna Sequencing Analysis. *Stem Cell Research & Therapy* **2022**, *13* (1), 187.
(69) Jalandhra, G. K.; Molley, T. G.; Hung, T.-t.; Roohani, I.; Kilian, K. A. In Situ Formation of Osteochondral Interfaces through "Bone-Ink" Printing in Tailored Microgel Suspensions. *Acta Biomaterialia* **2023**, *156*, 75−87.
(70) Xie, A.; Xue, J.; Wang, Y.; Yang, C.; Xu, M.; Jiang, Y. Kartogenin Induced Adipose-Derived Stem Cell Exosomes Enhance the Chondrogenic Differentiation Ability of Adipose-Derived Stem Cells. *Disease Markers* **2022**, *2022*, 1.
(71) Islam, M. S.; Molley, T. G.; Ireland, J.; Kruzic, J. J.; Kilian, K. A. Magnetic Nanocomposite Hydrogels for Directing Myofibroblast Activity in Adipose-Derived Stem Cells. *Advanced NanoBiomed Research* **2021**, *1* (4), 2000072.
(72) De Villiers, J. A.; Houreld, N.; Abrahamse, H. Adipose Derived Stem Cells and Smooth Muscle Cells: Implications for Regenerative Medicine. *Stem Cell Reviews and Reports* **2009**, *5*, 256−265.
(73) Park, J. S.; Chu, J. S.; Tsou, A. D.; Diop, R.; Tang, Z.; Wang, A.; Li, S. The Effect of Matrix Stiffness on the Differentiation of Mesenchymal Stem Cells in Response to Tgf-B. *Biomaterials* **2011**, *32* (16), 3921−3930.
(74) Hwang, J.-H.; Byun, M. R.; Kim, A. R.; Kim, K. M.; Cho, H. J.; Lee, Y. H.; Kim, J.; Jeong, M. G.; Hwang, E. S.; Hong, J.-H. Extracellular Matrix Stiffness Regulates Osteogenic Differentiation through Mapk Activation. *PloS one* **2015**, *10* (8), No. e0135519.
(75) Patel, M.; Koh, W.-G. Composite Hydrogel of Methacrylated Hyaluronic Acid and Fragmented Polycaprolactone Nanofiber for Osteogenic Differentiation of Adipose-Derived Stem Cells. *Pharmaceutics* **2020**, *12* (9), 902.
(76) Arjmand, M.; Ardeshirylajimi, A.; Maghsoudi, H.; Azadian, E. Osteogenic Differentiation Potential of Mesenchymal Stem Cells Cultured on Nanofibrous Scaffold Improved in the Presence of Pulsed Electromagnetic Field. *Journal of Cellular Physiology* **2018**, *233* (2), 1061−1070.
(77) Ganesh, N.; Ashokan, A.; Rajeshkannan, R.; Chennazhi, K.; Koyakutty, M.; Nair, S. V. Magnetic Resonance Functional Nano-Hydroxyapatite Incorporated Poly (Caprolactone) Composite Scaffolds for in Situ Monitoring of Bone Tissue Regeneration by Mri. *Tissue Engineering Part A* **2014**, *20* (19−20), 2783−2794.
(78) Yu, H.; Tay, C. Y.; Leong, W. S.; Tan, S. C. W.; Liao, K.; Tan, L. P. Mechanical Behavior of Human Mesenchymal Stem Cells During Adipogenic and Osteogenic Differentiation. *Biochemical and biophysical research communications* **2010**, *393* (1), 150−155.
(79) Long, E. G.; Buluk, M.; Gallagher, M. B.; Schneider, J. M.; Brown, J. L. Human Mesenchymal Stem Cell Morphology, Migration, and Differentiation on Micro and Nano-Textured Titanium. *Bioactive Materials* **2019**, *4*, 249−255.
(80) Zhao, Y.; Sun, Q.; Wang, S.; Huo, B. Spreading Shape and Area Regulate the Osteogenesis of Mesenchymal Stem Cells. *Tissue Engineering and Regenerative Medicine* **2019**, *16*, 573−583.
(81) Xu, J.; Li, Z.; Hou, Y.; Fang, W. Potential Mechanisms Underlying the Runx2 Induced Osteogenesis of Bone Marrow Mesenchymal Stem Cells. *Am. J. Transl. Res.* **2015**, *7* (12), 2527.
(82) Dalle Carbonare, L.; Innamorati, G.; Valenti, M. T. Transcription Factor Runx2 and Its Application to Bone Tissue Engineering. *Stem cell reviews and reports* **2012**, *8*, 891−897.
(83) Komori, T. Regulation of Osteoblast Differentiation by Transcription Factors. *Journal of cellular biochemistry* **2006**, *99* (5), 1233−1239.
(84) Kilian, K. A.; Bugarija, B.; Lahn, B. T.; Mrksich, M. Geometric Cues for Directing the Differentiation of Mesenchymal Stem Cells. *Proc. Natl. Acad. Sci. U. S. A.* **2010**, *107* (11), 4872−4877.
(85) Joshi, M. K.; Lee, S.; Tiwari, A. P.; Maharjan, B.; Poudel, S. B.; Park, C. H.; Kim, C. S. Integrated Design and Fabrication Strategies for Biomechanically and Biologically Functional Pla/B-Tcp Nanofiber Reinforced Gelma Scaffold for Tissue Engineering Applications. *Int. J. Biol. Macromol.* **2020**, *164*, 976−985.
(86) Betriu, N.; Jarrosson-Moral, C.; Semino, C. E. Culture and Differentiation of Human Hair Follicle Dermal Papilla Cells in a Soft 3d Self-Assembling Peptide Scaffold. *Biomolecules* **2020**, *10* (5), 684.
(87) Legzdina, D.; Romanauska, A.; Nikulshin, S.; Kozlovska, T.; Berzins, U. Characterization of Senescence of Culture-Expanded Human Adipose-Derived Mesenchymal Stem Cells. *International Journal of Stem Cells* **2016**, *9* (1), 124−136.
(88) Nii, M.; Lai, J. H.; Keeney, M.; Han, L.-H.; Behn, A.; Imanbayev, G.; Yang, F. The Effects of Interactive Mechanical and Biochemical Niche Signaling on Osteogenic Differentiation of Adipose-Derived Stem Cells Using Combinatorial Hydrogels. *Acta Biomaterialia* **2013**, *9* (3), 5475−5483.
(89) Vuornos, K.; Ojansivu, M.; Koivisto, J. T.; Häkkänen, H.; Belay, B.; Montonen, T.; Huhtala, H.; Kääriäinen, M.; Hupa, L.; Kellomäki, M.; et al. Bioactive Glass Ions Induce Efficient Osteogenic Differentiation of Human Adipose Stem Cells Encapsulated in Gellan Gum and Collagen Type I Hydrogels. *Materials Science and Engineering: C* **2019**, *99*, 905−918.
(90) Fang, X.; Murakami, H.; Demura, S.; Hayashi, K.; Matsubara, H.; Kato, S.; Yoshioka, K.; Inoue, K.; Ota, T.; Shinmura, K.; Tsuchiya, H. A Novel Method to Apply Osteogenic Potential of Adipose Derived Stem Cells in Orthopaedic Surgery. *PLoS One* **2014**, *9* (2), No. e88874.
(91) Kim, S. E.; Lee, D.-W.; Yun, Y.-P.; Shim, K.-S.; Jeon, D. I.; Rhee, J.-K.; Kim, H.-J.; Park, K. Heparin-Immobilized Hydroxyapatite Nanoparticles as a Lactoferrin Delivery System for Improving Osteogenic Differentiation of Adipose-Derived Stem Cells. *Biomedical Materials* **2016**, *11* (2), 025004.
(92) Leder, B. Z.; Wein, M. N. *Osteoporosis: Pathophysiology and Clinical Management*; Springer Nature: 2020.
(93) McColloch, A.; Rabiei, M.; Rabbani, P.; Bowling, A.; Cho, M. Correlation between Nuclear Morphology and Adipogenic Differentiation: Application of a Combined Experimental and Computational Modeling Approach. *Sci. Rep.* **2019**, *9* (1), 1−13.
(94) Mor-Yossef Moldovan, L.; Lustig, M.; Naftaly, A.; Mardamshina, M.; Geiger, T.; Gefen, A.; Benayahu, D. Cell Shape Alteration During Adipogenesis Is Associated with Coordinated Matrix Cues. *Journal of cellular physiology* **2019**, *234* (4), 3850−3863.
(95) Fujita, S.; Shimizu, H.; Suye, S.-i. Control of Differentiation of Human Mesenchymal Stem Cells by Altering the Geometry of Nanofibers. *Journal of Nanotechnology* **2012**, *2012*, 1.
(96) Titushkin, I.; Sun, S.; Paul, A.; Cho, M. Control of Adipogenesis by Ezrin, Radixin and Moesin-Dependent Biomechanics Remodeling. *J. Biomech.* **2013**, *46* (3), 521−526.

https://doi.org/10.1021/acsami.3c07021
ACS Appl. Mater. Interfaces XXXX, XXX, XXX−XXX

(97) Prentice, K. J.; Saksi, J.; Hotamisligil, G. S. Adipokine Fabp4 Integrates Energy Stores and Counterregulatory Metabolic Responses. *J. Lipid Res.* **2019**, *60* (4), 734−740.
(98) Liu, L.; Liu, H.; Chen, M.; Ren, S.; Cheng, P.; Zhang, H. Mir-301b∼ Mir-130b—Pparγ Axis Underlies the Adipogenic Capacity of Mesenchymal Stem Cells with Different Tissue Origins. *Sci. Rep.* **2017**, *7* (1), 1−8.
(99) Furuhashi, M.; Saitoh, S.; Shimamoto, K.; Miura, T. Fatty Acid-Binding Protein 4 (Fabp4): Pathophysiological Insights and Potent Clinical Biomarker of Metabolic and Cardiovascular Diseases. *Clinical Medicine Insights: Cardiology* **2014**, *8*, CMC.S17067.
(100) Chun, T.-H. Peri-Adipocyte Ecm Remodeling in Obesity and Adipose Tissue Fibrosis. *Adipocyte* **2012**, *1* (2), 89−95.
(101) Wang, L.; Johnson, J. A.; Zhang, Q.; Beahm, E. K. Combining Decellularized Human Adipose Tissue Extracellular Matrix and Adipose-Derived Stem Cells for Adipose Tissue Engineering. *Acta biomaterialia* **2013**, *9* (11), 8921−8931.
(102) Young, D. A.; Choi, Y. S.; Engler, A. J.; Christman, K. L. Stimulation of Adipogenesis of Adult Adipose-Derived Stem Cells Using Substrates That Mimic the Stiffness of Adipose Tissue. *Biomaterials* **2013**, *34* (34), 8581−8588.
(103) Costantini, M.; Testa, S.; Fornetti, E.; Barbetta, A.; Trombetta, M.; Cannata, S. M.; Gargioli, C.; Rainer, A. Engineering Muscle Networks in 3d Gelatin Methacryloyl Hydrogels: Influence of Mechanical Stiffness and Geometrical Confinement. *Frontiers in bioengineering and biotechnology* **2017**, *5*, 22.
(104) Kobayashi, N.; Yasu, T.; Ueba, H.; Sata, M.; Hashimoto, S.; Kuroki, M.; Saito, M.; Kawakami, M. J. E. h. Mechanical Stress Promotes the Expression of Smooth Muscle-Like Properties in Marrow Stromal Cells. *Experimental Hematology* **2004**, *32* (12), 1238−1245.
(105) Kurpinski, K.; Chu, J.; Hashi, C.; Li, S. Anisotropic Mechanosensing by Mesenchymal Stem Cells. *Proc. Natl. Acad. Sci. U.S.A.* **2006**, *103* (44), 16095−16100.
(106) Forcales, S.-V. Potential of Adipose-Derived Stem Cells in Muscular Regenerative Therapies. *Frontiers in Aging Neuroscience* **2015**, *7*, 123.
(107) Lawson, M. A.; Purslow, P. P. Differentiation of Myoblasts in Serum-Free Media: Effects of Modified Media Are Cell Line-Specific. *Cells Tissues Organs* **2000**, *167* (2−3), 130−137.
(108) Torgan, C. E.; Daniels, M. P. Regulation of Myosin Heavy Chain Expression During Rat Skeletal Muscle Development in Vitro. *Molecular biology of the cell* **2001**, *12* (5), 1499−1508.
(109) Heher, P.; Maleiner, B.; Prüller, J.; Teuschl, A. H.; Kollmitzer, J.; Monforte, X.; Wolbank, S.; Redl, H.; Rünzler, D.; Fuchs, C. A Novel Bioreactor for the Generation of Highly Aligned 3d Skeletal Muscle-Like Constructs through Orientation of Fibrin Via Application of Static Strain. *Acta biomaterialia* **2015**, *24*, 251−265.
(110) Tognato, R.; Armiento, A. R.; Bonfrate, V.; Levato, R.; Malda, J.; Alini, M.; Eglin, D.; Giancane, G.; Serra, T. A Stimuli-Responsive Nanocomposite for 3d Anisotropic Cell-Guidance and Magnetic Soft Robotics. *Adv. Funct. Mater.* **2019**, *29* (9), 1804647.
(111) Zhuang, P.; An, J.; Chua, C. K.; Tan, L. P. Bioprinting of 3d in Vitro Skeletal Muscle Models: A Review. *Materials & Design* **2020**, *193*, 108794.
(112) Ge, X.; Zhang, Y.; Park, S.; Cong, X.; Gerrard, D. E.; Jiang, H. Stac3 Inhibits Myoblast Differentiation into Myotubes. *PLoS One* **2014**, *9* (4), No. e95926.
(113) Pajcini, K. V.; Pomerantz, J. H.; Alkan, O.; Doyonnas, R.; Blau, H. M. Myoblasts and Macrophages Share Molecular Components That Contribute to Cell-Cell Fusion. *J. Cell Biol.* **2008**, *180* (5), 1005−1019.
(114) Wang, P. Y.; Thissen, H.; Tsai, W. B. The Roles of Rgd and Grooved Topography in the Adhesion, Morphology, and Differentiation of C2c12 Skeletal Myoblasts. *Biotechnology and bioengineering* **2012**, *109* (8), 2104−2115.
(115) Kim, M. S.; Jun, I.; Shin, Y. M.; Jang, W.; Kim, S. I.; Shin, H. The Development of Genipin-Crosslinked Poly (Caprolactone)(Pcl)/Gelatin Nanofibers for Tissue Engineering Applications. *Macromol. Biosci.* **2010**, *10* (1), 91−100.
(116) Li, Y.; Huang, G.; Gao, B.; Li, M.; Genin, G. M.; Lu, T. J.; Xu, F. Magnetically Actuated Cell-Laden Microscale Hydrogels for Probing Strain-Induced Cell Responses in Three Dimensions. *NPG Asia Materials* **2016**, *8* (1), No. e238.
(117) Mao, W.; Lee, S.; Kim, S.-R.; Kim, K.-N.; Yoo, H. S. Electrospun Nanohybrid Hydrogels for Enhanced Differentiation of Myoblasts. *Journal of Industrial and Engineering Chemistry* **2019**, *80*, 838−845.

https://doi.org/10.1021/acsami.3c07021
ACS Appl. Mater. Interfaces XXXX, XXX, XXX−XXX